Mars aerosol studies with the MGS TES emission phase function observations: Optical depths, particle sizes, and ice cloud types versus latitude and solar longitude

R. Todd Clancy and Michael J. Wolff
Space Science Institute, Boulder, Colorado, USA

Philip R. Christensen
Department of Geology, Arizona State University, Tempe, Arizona, USA

Received 5 February 2003; revised 23 April 2003; accepted 15 May 2003; published 3 September 2003.

[1] Emission phase function (EPF) observations taken in 1999–2001 by Mars Global Surveyor Thermal Emission Spectrometer (MGS TES) support the broadest study of Martian aerosol properties to date. TES solar band and infrared (IR) spectral EPF sequences are analyzed to obtain first-time seasonal/latitudinal distributions of visible optical depths, particle sizes, and single scattering phase functions. This combined angular and wavelength coverage enables identification of two distinct ice cloud types over 45°S–45°N. Type 1 ice clouds exhibit small particle sizes (r_{eff} = 1–2 μm) and a distinctive backscattering increase. They are most prevalent in the southern hemisphere during aphelion, but also appear more widely distributed in season and latitude as topographic and high-altitude (≥20 km) ice hazes. Type 2 ice clouds exhibit larger particle sizes (r_{eff} = 3–4 μm), a distinct side-scattering minimum at 90–100° phase angles (characteristic of a change in particle shape relative to the type 1), and appear most prominently in the northern subtropical aphelion cloud belt. The majority of retrieved dust visible-to-IR optical depth ratios are indicative of r_{eff} = 1.5 ± 0.1 μm, consistent with Pathfinder and Viking/Mariner 9 reanalyses. However, increased ratios (2.7 versus 1.7) appear frequently in the northern hemisphere over L_S = 50–200°, indicating substantially smaller dust particles sizes (r_{eff} = 1.0 ± 0.2 μm) at this time. In addition, larger (r_{eff} = 1.8–2.5 μm) dust particles were observed locally in the southern hemisphere during the peak of the 2001 global dust storm. Detailed spectral modeling of the TES visible band pass indicates agreement of EPF-derived dust single scattering albedos (0.92–0.94) with the spectrally resolved results from Pathfinder observations. *INDEX TERMS:* 0305 Atmospheric Composition and Structure: Aerosols and particles (0345, 4801); 0360 Atmospheric Composition and Structure: Transmission and scattering of radiation; 6225 Planetology: Solar System Objects: Mars; *KEYWORDS:* Martian atmosphere, aerosols, radiative transfer, remote sensing, dust and cloud optical depths

Citation: Clancy, R. T., M. J. Wolff, and P. R. Christensen, Mars aerosol studies with the MGS TES emission phase function observations: Optical depths, particle sizes, and ice cloud types versus latitude and solar longitude, *J. Geophys. Res.*, *108*(E9), 5098, doi:10.1029/2003JE002058, 2003.

1. Introduction

[2] The roles of aerosols in the Mars atmosphere and climate are fundamental on several levels. Even prior to the seminal Mariner 9 mission, radiative forcing from atmospheric dust solar absorption and thermal emission was recognized as a primary factor in the thermal structure of the global Mars atmosphere [*Gierasch and Goody*, 1972]. Mariner 9 and Viking observations during the intense global dust storm seasons of 1971 and 1977 identified the strong, vertically deep, and very abrupt forcing on global circulation associated with perihelion dust storm activity [*Zurek*, 1982; *Kahn et al.*, 1992]. Recently, Mars global circulation models (MGCM) have made great progress in simulating the meridional and vertical evolutions of atmospheric circulation associated with global dust storms [*Haberle et al.*, 1982; *Wilson*, 1997], but are still hampered by insufficient data bases for dust optical and physical properties. Of key importance are the seasonally/spatially variable aerosol composition (ice and dust components), single scattering phase and albedo functions versus wavelength, and particle

0148-0227/03/2003JE002058$09.00

sizes and shapes. It has also been proposed that the nonlinear microphysics of dust-ice aerosol interactions play an active role in the latitudinal and annual variations of aerosol and water vapor distributions and their cross-hemispheric transport [*Clancy et al.*, 1996]. Addressing these fundamental climate issues require accurate observational definitions of the separate dust and ice optical and physical properties versus season and latitude.

[3] Existing studies of Mars aerosol properties have been constrained by the limited angular/wavelength coverage of global spacecraft observations, and the limited spatial/wavelength coverage of lander observations. Viking and Pathfinder solar extinction measurements from the surface of Mars still constitute the most accurate determinations of aerosol optical depths [*Colburn et al.*, 1989; *Smith and Lemmon*, 1999]. The long baseline of the Viking lander measurements and the daily/diurnal coverage afforded by both lander missions lend these data to unique meteorological studies of their specific landing sites [*Haberle et al.*, 1999]. The Pathfinder near-Sun imaging of the aerosol forward scattering peak also yields the most accurate determination of dust particle sizes [*Tomasko et al.*, 1999]. However, the relative contributions of ice and dust hazes are not well separated in these lander aerosol measurements. Neither the Viking nor Pathfinder lander mission provided diagnostic spectral observations in the near or thermal infrared regions, such that lander aerosol analyses have relied upon diurnal and spatial (waveform) variations to assess ice cloud contributions. The local nature of these lander investigations further handicaps ice haze identification and severely limits their application in global studies.

[4] Viking thermal infrared band photometry with the IRTM experiment generated global measurements of infrared dust optical depths (e.g., 9 μm [*Martin*, 1986]) for more than one Mars year (1977–1980). The Mariner 9 IRIS experiment yielded unambiguous spectral identifications of the ice and dust infrared absorptions [*Hanel et al.*, 1972], as well limited particle size constraints for both dust and ice aerosols. The 9–30 μm spectrum of atmospheric dust constrains the 1–5 μm radii particle size distribution [*Toon et al.*, 1977], but is subject to uncertainty in the wavelength-dependent surface emissivity of Mars [*Clancy et al.*, 1995]. Visible-to-infrared (9 μm) opacity ratios from coincident Viking lander and IRTM observations [*Martin*, 1986; *Clancy et al.*, 1995] indicate substantially (factor of two) smaller dust particle sizes than interpreted from the earlier Mariner 9 [*Toon et al.*, 1977] and Viking lander [*Pollack et al.*, 1979] analyses. Such smaller particle sizes are also consistent with the near-infrared Phobos limb observations [*Chassefiere et al.*, 1992], Viking lander reanalyses [*Pollack et al.*, 1995] and the aforementioned Pathfinder imaging results. As yet, there are no quantitative measurements of spatial or seasonal variations in dust particle sizes, despite the fact that Mars global circulation models (MGCM) robustly predict such variations [*Murphy et al.*, 1993]. Current estimates of Mars ice aerosol particle sizes are based on Mariner 9 and MGS analyses of 12 μm absorption features observed for two volcanic summit ice clouds, which yield estimates of 2 μm [*Curran et al.*, 1973] and 1–4 μm [*Pearl et al.*, 2001] particle radii, respectively. In addition, Phobos near infrared limb observations of 20–30 km altitude ice hazes indicate 2 μm ice particle radii [*Rodin et al.*, 1997].

[5] The MGS TES experiment, although designed as a surface mineralogical investigation [*Christensen et al.*, 1998, 2001], has already expanded our Mars aerosol data base several fold. Parts of three Mars years have now been observed, in which accurate dust and water ice thermal infrared optical depths (9 and 12 μm) have been mapped in detail [*Christensen et al.*, 2001; *Smith et al.*, 2001; *Pearl et al.*, 2001]. In its first two years of operation, MGS observed perihelion conditions of relatively moderate dust loading, characterized by regional rather than global (planet-encircling) dust storm activity. The TES aerosol mapping data further show that the seasonal (Mars solar longitude, L_S) and latitude character of such moderate perihelion dust conditions can exhibit remarkable repeatability over two consecutive perihelion seasons [*Smith et al.*, 2001]. However, a global or planet-encircling dust storm began at $L_S = 185°$ of June 26 of 2001, an unprecedented early season for global dust storm generation [*Martin and Zurek*, 1993]. TES dust and temperature soundings over the course of this global dust storm are presented by *Smith et al.* [2002].

[6] TES water ice aerosol mapping has now defined the full annual variation water ice aerosol optical depths for the first time [*Pearl et al.*, 2001; *Smith et al.*, 2001]. The discovery of a global aphelion cloud belt through ground-based spectroscopic and HST imaging observations [*Clancy et al.*, 1996] points out notable gaps in pre-MGS Mars water ice aerosol observations, which have focused on discrete cloud forms as meteorological indicators [*French et al.*, 1981; *Kahn*, 1984]. The Mariner 9, Viking, and Phobos orbiter observations failed to define this global ice haze structure for various reasons. Mariner 9 IRIS did not operate frequently enough in the aphelion season, the Viking IRTM absorption band measurement is less sensitive to ice aerosol absorption, and the Phobos limb observations were too limited in time and space. Subsequent Pathfinder aerosol investigations also did not identify the aphelion cloud belt, partly due to unfortunate timing (landing just as the cloud belt decayed). However, the visible imaging systems on the Viking and Pathfinder landers were not suited to spectral discrimination of ice and dust aerosols. The TES infrared spectral analyses of water ice absorption (12 μm [*Pearl et al.*, 2001; *Smith et al.*, 2001]) have now confirmed the global scale and persistence of the aphelion ice cloud phenomenon. It has also been confirmed for the 1999 aphelion by ground-based imaging spectroscopy in the near IR [*Glenar et al.*, 2003]. Finally, a sensitive reanalysis of the Viking IRTM 11 μm observations shows that this cloud belt was in fact present during the Viking aphelion periods [*Tamppari et al.*, 2000].

[7] Definitions of Mars water ice aerosol properties for aphelion and nonaphelion ice clouds are a major thrust of the TES emission phase function (EPF) analyses presented here and in a companion paper by *Wolff and Clancy* [2003]. We employ solar band scattering and infrared spectral absorption measurements within TES EPF sequences to investigate global-scale variations in the physical properties (size, shape, and ice versus dust) of Mars aerosols, as a function of L_S and latitude. Our approach is to derive a

minimum set of Mars aerosol types that satisfy the full range of TES EPF wavelength and emission/scattering constraints obtained over the 45°S–45°N latitude region for more than one Mars year (1998–2001). We model the detailed spectral weighting of the TES solar band channel (0.3–3.0 μm) to facilitate self-consistent comparisons with existing narrow-band visible measurements of dust physical and optical properties from the Viking and Pathfinder imaging experiments. Coincident TES infrared spectra are employed as a qualitative dust-versus-ice indicator in support of the multiple scattering RT analysis of each solar band EPF sequence. We also compare TES dust and ice IR optical depths with TES solar band optical depths to characterize the behavior of ice particle size as a function of aerosol scattering type, L_S, and latitude. IR absorption optical depths for dust and ice from *Smith et al.* [2001] are compared for each solar band EPF analyzed. The multiple scattering analysis of TES infrared spectra by *Wolff and Clancy* [2003] for a subset of the analyzed solar band EPF sequences provides visible/IR extinction optical depth ratios. These allow quantitative measurements of aerosol particle sizes, which we compare with independent aerosol particle sizes derived from the IR spectral analysis of *Wolff and Clancy* [2003] for the most complete study of Mars aerosol particle sizes to date.

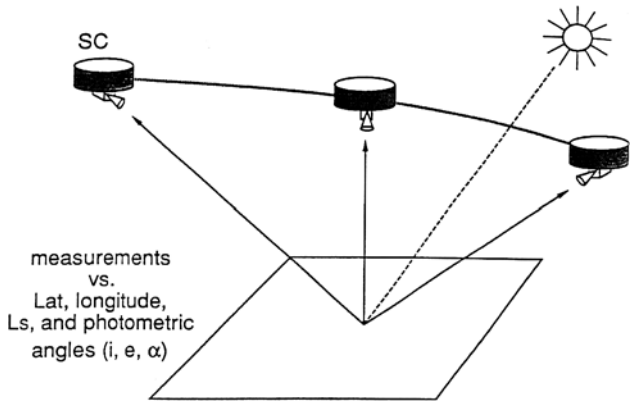

Figure 1. Schematic representation of an emission phase function (EPF) sequence, as observed from the MGS orbiter. The solar incidence angle at the targeted surface location remains nearly constant as the emission angle viewed from the spacecraft (SC) varies from −75° (approaching SC), to 0° (nadir SC), to +75° (receding SC). The solar phase angle typically varies by 70° within a given EPF sequence (reproduced from *Clancy and Lee* [1991]).

2. Data Analysis

2.1. TES EPF Description

[8] Mapping (orbital) retrievals for visible aerosol optical depths are much more difficult to obtain than for thermal absorption optical depths, due to the complex scattering phase behavior of dust and ice aerosols. Ultraviolet/visible aerosol optical depths have been derived from Mariner 9 [*Pang and Hord*, 1973], Viking [*Thorpe*, 1979, 1981], and Mars Global Surveyor [*Cantor et al.*, 2001; *Ivanov and Muhleman*, 1998] nadir brightness measurements, but are generally inaccurate for dust aerosols and indiscriminate for dust versus ice aerosols. A more quantitative approach is provided by the extensive angular coverage of emission phase function (EPF) sequences, which allow the required separation of surface scattering and discrimination of the aerosol single scattering phase function [*Clancy and Lee*, 1991]. Analysis of Viking IRTM EPF sequences provided accurate solar band optical depths, which compared well with coincident Viking lander measurements and allowed first-time direct comparisons of visible and thermal infrared aerosol optical depths [*Clancy et al.*, 1995]. However, Viking IRTM EPF sequences were quite limited in spatial and seasonal coverage. The TES EPF data set provides full climatological (seasonal and spatial) coverage complemented with diagnostic thermal infrared spectroscopy [*Christensen et al.*, 1998, 2001], and so affords significant advancements in our understanding of Mars aerosol properties and behaviors.

[9] Figure 1 presents a schematic of the observing geometry for EPF sequences, where the surface and atmospheric scattering above a point on the Mars surface are observed through a large range of scattering/emission angles as the spacecraft passes overhead. TES scans only within the orbit plane as compared to the two axis pointing capability of the Viking IRTM experiment. Consequently, rotation of Mars during the 1 minute period of the −75° to +75° emission angle coverage of TES leads to several degree longitudinal spread in each TES EPF sequence. The specific angular, seasonal, and spatial coverages of the TES EPF observations evolved over the MGS primary mission. During the first half of the mapping mission, TES EPF sequences were obtained once per orbit, incremented in 15 degrees of latitude between 60 north and south latitudes, with irregular and sparse longitudinal coverage, and for emission angles of ±75°, ±55°, and 0°. Currently, TES EPF sequences are obtained twice per orbit, incremented in 7.5 degrees of latitude between 90 north and south latitudes, with improved but still nonuniform longitudinal coverage, and for emission angles of ±75°, ±65°, ±55°, ±30°, and 0°.

[10] Figure 2 presents a typical 5-emission-angle TES EPF sequence, where the observed EPF reflectances are represented by "plus" symbols. The model fits (lines) correspond to three best-fit aerosol optical depths (τ) and surface albedos (Alb) for several distinct aerosol scattering models (line types) with specified single scattering phase functions and albedos (SSA), as described in following sections. Figure 3 shows a "dense" EPF sequence, in which nearly continuous emission angle coverage is measured (once per day) to provide a finer angular definition of the aerosol scattering behavior. Figures 2 and 3 present cases of predominantly dust scattering, as determined both by the scattering model which best fits the data (e.g., the "Pathfinder dust" in Figure 2) and the TES infrared spectra associated with each EPF sequence (see below). In terms of the observed EPF reflectance dependence on emission angle, the increased path length of the aerosol scattering at higher emission angles leads to increased atmospheric reflectance for emission angles beyond 55–65°. Low emission angles are most sensitive to the surface albedo, particularly for the low dust loading conditions typical of the MGS observational period.

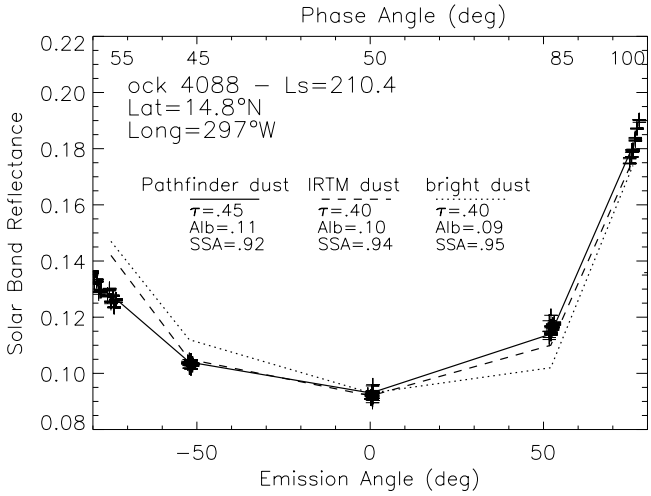

Figure 2. TES EPF sequence obtained on ock 4088 for the latitude, L_S, longitude coordinates as labeled. The data are represented by plus symbols, with approximately 30 measurements at each the 5 distinct emission angles observed for this early mission sequence. Corresponding phase angles of observation are indicated at the top horizontal axis. The solar band reflectances have not been scaled to account for the nonzero incidence angle (47°). Model EPF sequences for the same set of emission, phase, incidence angles are presented for three models of dust scattering behavior (as described in text). The best-fit dust optical depth (τ) and surface normal reflectance (Alb) are indicated for each model fit. In this case, the EPF observation is best represented by the Pathfinder model of dust scattering [*Tomasko et al.*, 1999].

[11] The EPF emission angle coverage also incorporates significant scattering (or phase) angle variations, which lead to emission angle brightness variations associated with the aerosol single scattering phase function. The range of phase angle coverage viewed depends upon the latitude and season (L_S) of the observation. Minimum and maximum phase angles observed from MGS are 25° and 150°, respectively. Typical phase angle coverage in a given low-to-mid latitude EPF sequence is 30° to 100°, such that EPF sequences are most determinant of the side scattering behavior of Mars aerosols. The asymmetric emission angle dependence of brightening indicated in Figure 2 results from the increasingly forward-scattering angles presented, in this case, at the positive emission angles. The phase angle coverage for each presented EPF sequence is indicated on the top horizontal scale. Figures 4 and 5 present typical nine-point EPF sequences for two distinctive types of Mars ice clouds, both of which are characterized by phase scattering variations at 60–120° phase angles. Such ice aerosol phase function scattering often exhibits peak EPF brightnesses at intermediate, versus maximum emission angles (e.g., 40–60° in Figures 4 and 5, versus ±75° in Figure 3), which distinguish EPF sequences for predominantly ice versus dust aerosol conditions. Figures 4 and 5 include best-fit optical depth fits for dust as well as ice aerosol scattering models, to indicate the dependence of the goodness of fit with the assumed aerosol scattering phase function. As demonstrated by *Clancy and Lee* [1991] and the current analysis, solar band EPF sequences can display sensitivity to the aerosol single scattering albedo (SSA) for moderate to high dust loading conditions over bright surface regions. However, this dependence is typically weak such that we fix single scattering albedos according to the aerosol scattering type (ice versus dust) which best fits the solar band EPF sequence and provides consistency with the TES infrared spectra in terms of relative dust and ice absorption depths.

2.2. Model Description

[12] Radiative transfer modeling of the TES solar band EPF sequences is conducted with an updated version of the discrete ordinate code DISORT [*Stamnes et al.*, 1988] employed in the Viking EPF analysis by *Clancy and Lee* [1991]. Primary attributes of this multiple scattering code are specification of a bidirectional surface reflection, angular discretization of the intensity field, and vertical discretization of the atmosphere. The angular dependences of the surface and aerosol scattering phase functions are input as Legendre polynomial expansions, as required by the Stamnes et al. code. We employ 64 streams and hence 64 Legendre coefficients to represent the angular distributions of atmospheric and surface scattering. These include the input of aerosol single scattering phase functions, which are not fit individually for each EPF sequence (see below), nor

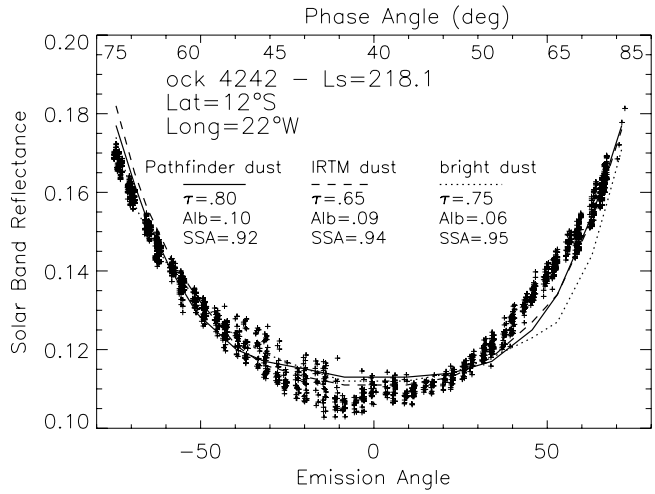

Figure 3. TES EPF sequence obtained on ock 4242 for the latitude, L_S, longitude coordinates as labeled. The data are represented by plus symbols, obtained over an effectively continuous range of emission angles observed for an atypical, dense emission angle sequence. Corresponding phase angles of observation are indicated at the top horizontal axis. The solar band reflectances have not been scaled to account for the nonzero incidence angle (38°). Model EPF sequences for 18 values of emission, phase, incidence angle are presented for three models of dust scattering behavior (as described in text). The best-fit dust optical depth (τ) and surface normal reflectance (Alb) are indicated for each model fit. In this case, the EPF observation does not clearly discriminate between the Pathfinder [*Tomasko et al.*, 1999] or the Viking IRTM EPF [*Clancy and Lee*, 1991] models of dust scattering.

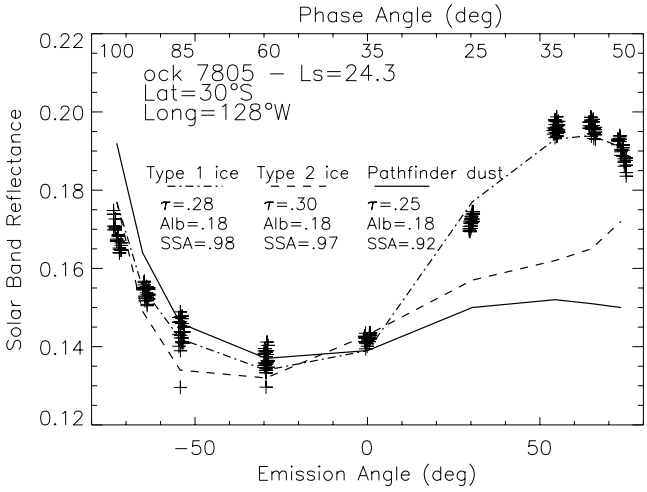

Figure 4. TES EPF sequence obtained on ock 7805 for the latitude, L_S, longitude coordinates as labeled. The data are represented by plus symbols, with approximately 30 measurements at each the 9 distinct emission angles observed for this typical mapping mission sequence. Corresponding phase angles of observation are indicated at the top horizontal axis. The solar band reflectances have not been scaled to account for the nonzero incidence angle (47°). Model EPF sequences for the same set of emission, phase, incidence angles are presented for two models of ice and one model of dust scattering behavior (as described in text). The best-fit ice or dust optical depth (τ) and surface normal reflectance (Alb) are indicated for each model fit. In this case, the type 1 ice scattering phase function provides the best representation of the observed EPF behavior.

constrained at the level of this input resolution (~3 degrees) or coverage. In particular, the TES EPF sequences do not directly constrain aerosol scattering at phase angles greater than 150° (and, typically, greater than 120°). However, accurate modeling of the narrow forward scattering peak of Mars aerosols optimizes the model accuracy of atmospheric multiple scattering and provides self-consistent comparisons with the dust scattering phase function retrieved from the Pathfinder forward scattering analysis [*Tomasko et al.*, 1999]. For Mars surface phase behavior, we adopt the dark and bright region surface phase functions determined from the *Clancy and Lee* [1991] Viking EPF analysis. The Viking EPF sequences, although restricted in spatial and seasonal coverage, include phase coverage near zero degrees due to variable local time coverage from the Viking orbiters. Apart from the 0–20° opposition behavior of the Mars surface reflectance which MGS does not observe, the phase variation of surface reflection is small relative to the atmospheric phase and emission angle variation present in EPF sequences [see *Clancy and Lee*, 1991].

[13] Aerosol optical depths and single scattering albedos are specified for three vertical layers (0–10 km, 10–20 km, 20–50 km) to account for potential ice and dust vertical layering effects in specific cases of multiple component aerosol models, such as ice clouds confined above the dust aerosols. However, such multicomponent aerosol models are constructed for only a small subset of TES EPF solar band sequences, where the *Wolff and Clancy* [2003] analysis of coincident TES infrared spectra allows specific separations of the dust and ice components. For the majority of the TES solar band EPF sequences presented here, we have used only single aerosol type models as described below, in which case there is no sensitivity to the aerosol vertical distribution. We also note that aerosol optical depths retrieved from single aerosol type models agree to within 10% of those derived for the total optical depths found in the corresponding multicomponent analysis. In other words, the aerosol optical depths retrieved by single versus multicomponent solutions are very nearly the same. This agreement follows from the fact that the average visible single scattering cross section for the aerosol types (i.e., dust versus ice) is comparable when averaged over the observed range of phase angles fit for each EPF sequence.

[14] We ignore the weak gas scattering and absorption present at visible/near IR wavelengths, although detailed gas transmission spectra are incorporated in our sensitivity analysis of atmospheric spectral variation across the TES solar band channel. As with the previous IRTM EPF analysis of *Clancy and Lee* [1991], we analyze the TES solar band (0.3–3.0 μm) EPF reflectance as a single channel (approximately red) measurement. The TES solar band channel provides roughly constant throughput over the 0.4 to 2.8 μm wavelength region (light solid line in Figure 6), but in terms of surface and atmospheric reflection, it is further weighted by the solar irradiance (light dotted line

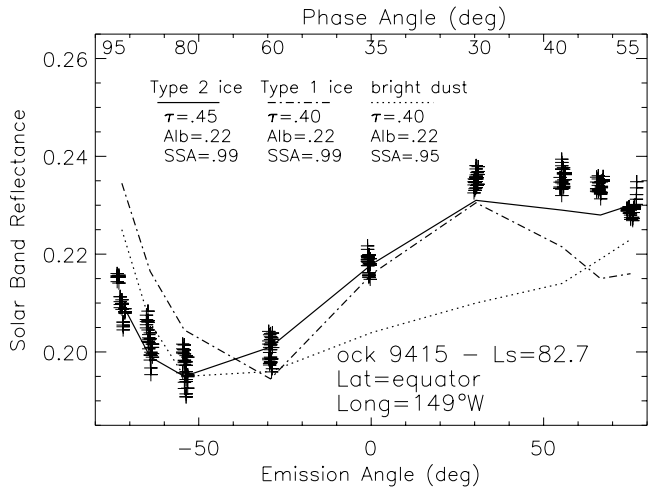

Figure 5. TES EPF sequence obtained on ock 9415 for the latitude, L_S, longitude coordinates as labeled. The data are represented by plus symbols, with approximately 30 measurements at each the 9 distinct emission angles observed for this typical mapping mission sequence. Corresponding phase angles of observation are indicated at the top horizontal axis. The solar band reflectances have not been scaled to account for the nonzero incidence angle (36°). Model EPF sequences for the same set of emission, phase, incidence angles are presented for two models of ice and one model of dust scattering behavior (as described in text). The best-fit ice or dust optical depth (τ) and surface normal reflectance (Alb) are indicated for each model fit. In this case, the type 2 ice scattering phase function provides the best representation of the observed EPF behavior.

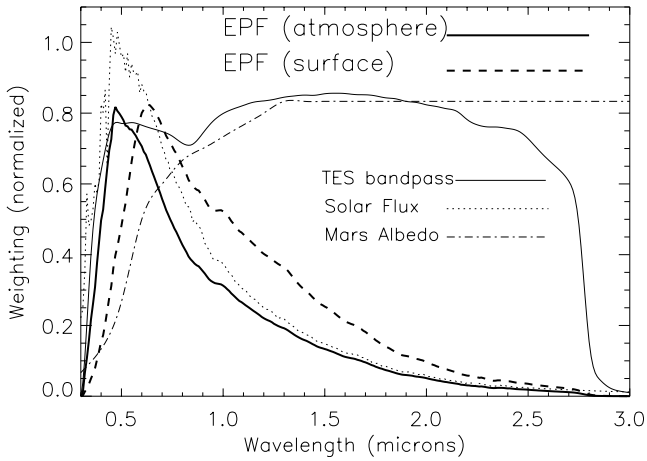

Figure 6. Spectral radiance weighting of the TES solar band channel, as influenced by the solar spectrum (dotted line), the TES solar band pass (thin solid line), and the surface reflectance for a moderately bright region on Mars (red albedo = 0.17, dash-dotted line). The net effective spectral weighting of the TES solar band channel is shown for predominantly atmospheric scattering (e.g., EPF reflectance at high emission angles, thick solid line) and for predominately surface scattering (e.g., zero emission angles for low-to-moderate atmospheric aerosol loading, thick dashed line).

in Figure 6) and the (wavelength-dependent) surface reflectance (dash-dotted line in Figure 6). The effective wavelength-weighting of TES solar band measurements may vary slightly from pure surface reflection (heavy dashed line in Figure 6; e.g., nadir) to predominantly atmospheric/aerosol reflection (heavy solid line in Figure 6; e.g., high emission angle). We establish the effective wavelength range (0.5–1.5 μm) and mean wavelength (0.7 μm) for our EPF-derived aerosol opacities and absorption properties based on spectral models of dust and ice scattering and absorption cross sections over the TES solar band pass (as presented below). Our spectral analysis includes full RT calculations versus wavelength (at 0.01 μm resolution), self-consistent wavelength dependences for aerosol and gas absorption/scattering and surface reflectance, and appropriate instrumental and solar flux weightings for band-pass averaging (Figure 6). This analysis also facilitates quantitative cross comparisons of EPF-derived dust single scattering albedos with the visible single scattering albedo measurements from Pathfinder imaging [*Tomasko et al.*, 1999].

[15] The primary retrieval goals for this analysis are the definition of single scattering phase functions and physical properties for separate ice and dust aerosols (including two ice types), and the mapping of aerosol optical depths versus season (one full Mars year, but including a small set of dust retrievals during the 2001 global dust storm) and latitude (45°S to 45°N, where full seasonal coverage is possible). Our approach is to define a minimum set of aerosol phase functions that fits the observed range of aerosol scattering phase behavior. The separation of pure ice and dust phase functions is facilitated by presented atmospheric conditions of mostly ice or dust aerosols according to Mars season, and by the aerosol absorption characteristics present in the coincident TES infrared spectra. Because the RT problem is nonlinear and compounded with highly variable observational and atmospheric conditions, we interactively fit several hundred EPF sequences rather than attempt a blind least squares automated approach. We conduct preliminary iterative solutions for selected EPF sequences that span the complete range of atmospheric and observational conditions, in order to construct the basis set of aerosol phase functions. These model aerosol phase functions are simple trial and error, fit-by-eye solutions that are constructed at 3° angular resolution between 0 and 180° phase angles, and least squares fitted to 64 coefficient Legendre polynomials. We were able to limit the number of these model single scattering phase functions to five cases found to adequately fit the full range of analyzed EPF sequences.

[16] Upon selection of these phase function types (presented and discussed below), we best-fit each of the full set of analyzed EPF sequences (~350) with 3–4 of these basis aerosol phase functions most appropriate to the EPF sequence and its infrared spectrum. This allows a quantitative selection of aerosol type for each EPF sequence (again, with guidance from the observed TES infrared spectrum), and also provides an estimate of the error in the derived optical depth as contributed by uncertainty in the aerosol scattering phase function. In general, such modeling uncertainties (including separation of surface and aerosol scattering albedos, and our coarse treatment of the surface scattering phase function) dominate over measurement uncertainties (e.g., radiance noise and calibration uncertainties) in defining the total errors in the derived aerosol optical depths. These modeling uncertainties typically limit the accuracy of our solar-band optical depths to ±0.05 for optical depths between 0.20 and 0.50. Uncertainties are correspondingly smaller for very low optical depths, and larger (±0.1 to 0.3) for high optical depths. For visible optical depths greater than 1.5, the observed EPF brightnesses become increasingly dependent on the aerosol single scattering albedo and less sensitive to the total optical depth.

2.3. Spectral Variations Over the TES Solar Band Channel

[17] Here, we consider the effects of expected spectral variations across the TES solar band channel (Figure 6), especially with regard to the specific wavelength averaging and accuracies represented in the EPF retrieved aerosol properties and surface albedo. For this purpose, we adopt optical/physical models for Mars dust and ice aerosol populations in detailed RT calculations of dust and ice reflectance spectra over the 0.3 to 3.0 μm wavelength region. The model reflectance spectra are calculated at 0.01 μm resolution (but smoothed for presentation to 0.1 μm resolution) for accurate inclusion of gas (CO_2, H_2O, and CO) transmissions supplied by Michael Smith (personal communication, 2001). The model also employs Mie calculations of aerosol single scattering albedo (ssa) and extinction optical depth versus wavelength on the basis of dust optical constants as described by *Clancy et al.* [1995] and *Wolff and Clancy* [2003], water ice optical constants from *Warren* [1984], and a representative aerosol size distribution (r_{eff} = 1.5 μm, variance = 0.4 μm). We

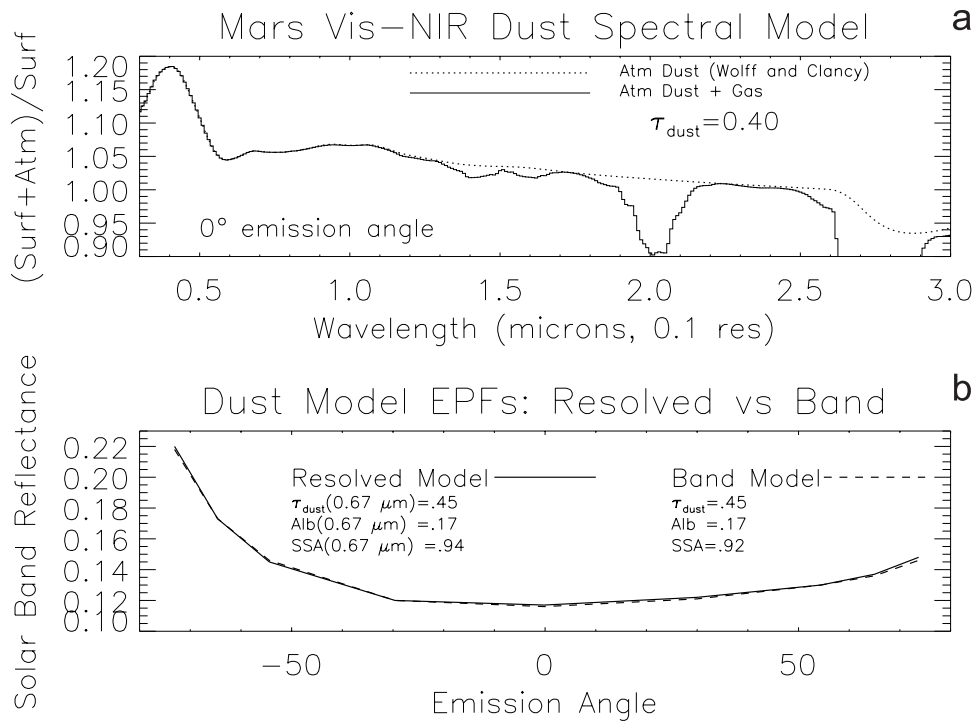

Figure 7. (a) Resolved spectral model for the visible-to-near IR reflectance of a "palagonite-like" dust aerosol (see text for discussion of dust optical model, $\tau = 0.4$) over a moderately bright (red albedo = 0.17) region on Mars. The solid and dotted line model spectra correspond to multiple scattering RT calculations with and without atmospheric gas transmission, respectively, at a zero emission angle. (b) Model comparisons for wavelength- independent (dashed line) versus spectrally integrated (solid line) RT calculations of a synthetic TES EPF sequence over a moderately bright surface for a dust optical depth of 0.45. The model fit parameters for the wavelength-dependent model are indicated for a wavelength of 0.67/micron/. The close agreement between the resolved and band models indicates the accuracy of the monochromatic RT fits adopted in the current analysis, and an effective wavelength near 0.7 μm for the retrieved aerosol optical depths, single scattering albedos, and surface reflectances (see Figure 9).

adopt fixed single scattering phase functions from the EPF analyses rather than the Mie wavelength-dependent models of scattering phase function, as such spherical phase calculations provide poor approximations to Mars aerosol phase scattering behavior. A coarse representation of surface albedo versus wavelength (Figure 6) for a moderately bright region is modeled in all of the resolved cases presented in this section.

[18] Figure 7a presents a model visible-near infrared spectrum of combined surface and atmosphere (i.e., aerosol) reflectance, as a ratio to the model surface-only reflectance (in this case, at an incidence angle of 53° and emission angle of 0°). The dust extinction optical depth is 0.45 at a wavelength of 0.7 μm, and the surface normal reflectance is as presented in Figure 6. The primary atmospheric gas absorption is contributed by 6 mbar of CO_2 gas, but the model also includes standard H_2O (10 precipitable microns) and CO (7 ppmv) trace absorptions. Gas absorption, which is dominated by CO_2 bands centered at 2.0 and 2.7 μm, is omitted in the model dust-only spectrum presented by the dashed line. The smoothly varying dust spectrum is distinguished by a weak hydration feature at 2.8 μm present in the palagonite sample that is the basis for the dust near IR optical constants, and a broad peak near 1 μm associated with 1.5 μm mean radius of the dust particle size distribution. The sharp rise in Figure 7a reflectance ratios shortward of 0.6 μm is a relative rather than absolute feature of dust aerosol reflectance, created by the much sharper increase in surface versus aerosol absorption within the iron charge transfer transition that characterizes Mars spectral reflectance over this wavelength region. This 0.4–0.5 μm peak in (atmosphere + surface)/surface dust reflectance ratios is a significant aspect of solar band EPF sensitivity to aerosol optical depth. When weighted by solar flux and the TES band pass, roughly one quarter of the solar band integrated increase in reflectance over surface-only scattering (corresponding to a "surf + atm/surf" value greater than 1.0 in Figure 7a) is contributed by aerosol scattering shortward of 0.5 μm.

[19] The enhancement of reflected visible and near IR radiation from atmospheric dust, as opposed to a surface-only reflection, is modest for the nadir geometry and relatively bright surface albedo conditions modeled in Figure 7a. However, the effects of atmospheric dust scattering become much more pronounced (and so the surface and atmosphere more separable) at large emission angles, as demonstrated in two model EPFs presented in Figure 7b. As discussed earlier, this is due both to increased atmospheric path lengths at large emission angles and increased aerosol scattering toward the forward scattering direction. This

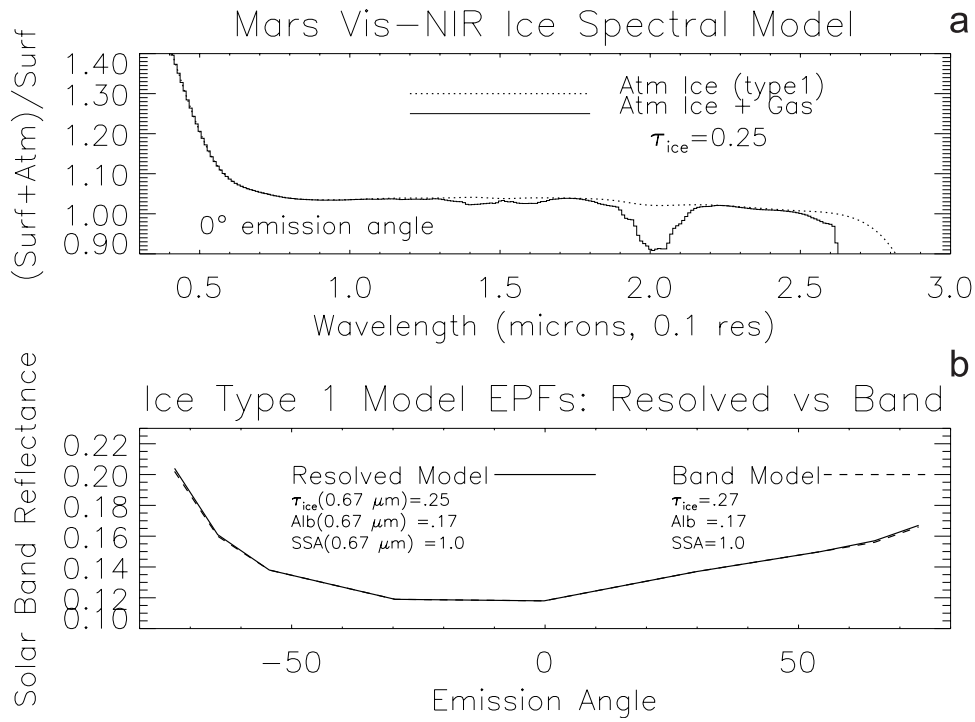

Figure 8. (a) Resolved spectral model for the visible-to-near IR reflectance of a type 1 ice aerosol (optical constants from *Warren* [1984], $\tau = 0.25$) over a moderately bright (red albedo = 0.17) region on Mars. The solid and dotted line model spectra correspond to multiple scattering RT calculations with and without atmospheric gas transmission, respectively, at a zero emission angle. (b) Model comparisons for wavelength-independent (dashed line) versus spectrally integrated (solid line) RT calculations of a synthetic TES EPF sequence over a moderately bright surface for a type 1 ice optical depth of 0.25. The agreement between these models indicates the accuracy of the monochromatic RT fits adopted in the current analysis, and an effective wavelength of 0.7 μm for the retrieved aerosol optical depths, single scattering albedos, and surface reflectances (see Figure 9).

second effect accounts for the rapid increase in brightness at high negative emission angles exhibited by the model EPFs of Figure 7b. The two cases presented compare nearly identical model EPF results for spectrally resolved (solid line) and single channel radiative transfer calculations (dashed line). Both models are calculated for 9 emission angles, from −73° to +74° emission angles, corresponding to a phase angle range from 115° to 40°. The resolved model (indicated by Figure 7a for 0° emission angle) is spectrally averaged with weighting provided by the solar spectrum and the TES band pass (Figure 6) to obtain a solar band integrated reflectance at each emission angle. The single channel model corresponds to the standard modeling approach (i.e., monochromatic) employed for all presented results of this paper.

[20] The close agreement between the spectrally resolved (solid line) and single channel (dashed line) dust model EPFs in Figure 7b is obtained for the dust parameters (optical depth and single scattering albedo) and surface reflectances indicated on Figure 7b. These parameters are equivalent at a wavelength of 0.67 μm for the spectrally resolved model. Figure 8a and 8b present type 1 ice model results for the visible-near IR reflectance spectrum and equivalent resolved versus single channel EPFs, respectively. Similar to the case of the Figure 7 dust comparisons, good agreement between the spectrally resolved and single channel EPF models for ice aerosol corresponds to an equivalent wavelength near 0.7 μm.

[21] Figure 9 presents the visible-near IR wavelength-dependence of the model (solid lines) for dust extinction optical depth, single scattering albedo, and surface normal reflectance. These model inputs correspond to the resolved dust EPF case in Figure 7. Also indicated on Figure 9 are the constant values (dashed lines) that yield equivalent EPF results (heavy dashed line in Figure 7b), and the effective TES wavelength-dependent weighting corresponding to aerosol scattering (Figures 9a and 9b) and surface scattering (Figure 9c). For all three properties indicated in Figure 9, correspondence between the equivalent single channel and wavelength-dependent (resolved) solution occurs at a wavelength near 0.7 μm. This is substantially shortward of the radiance-weighted mean wavelength for the TES solar band channel (1.0 μm). Such a blueward bias in the EPF effective wavelength reflects both the sharp decreases in aerosol and surface albedos below 0.6 μm (Figure 9) and rapidly increasing atmosphere-surface contrast at wavelengths below 0.6 μm (Figures 7a and 8a). Essentially identical conclusions apply to the resolved versus band average solutions for EPF ice aerosol analyses (Figure 8); although in this case the single scattering albedo remains unity shortward of the 2.8 μm ice absorption band. In summary, EPF

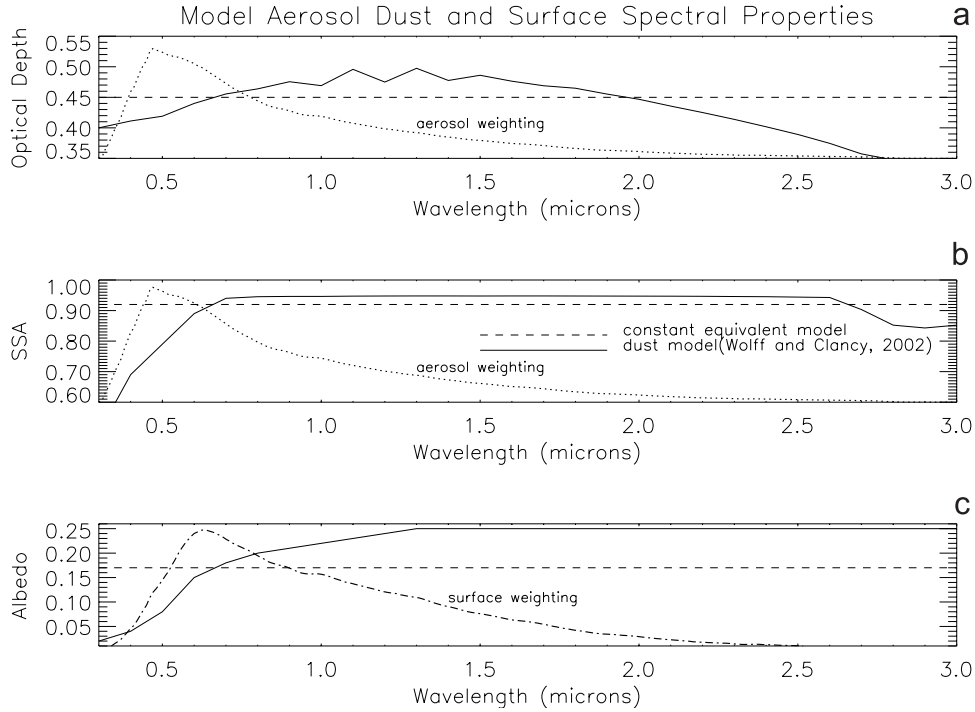

Figure 9. Model parameter comparisons between the spectrally resolved (solid lines) versus the wavelength-independent RT calculations (dashed lines) for the equivalent synthetic EPF sequences presented in Figure 7b. (a) Model dust optical depth as a function of wavelength for the Mie scattering "palagonitic" dust model of Figure 7a and 7b (solid line) versus the comparison monochromatic, band model (dashed line) of Figure 7b. The effective TES solar band weighting for atmospheric scattering in given by the dotted line. The wavelength-dependent versus independent solutions give equivalent dust optical depths at a wavelength of 0.7 μm. (b) Similar comparison for the dust single scattering albedo. Agreement between the equivalent EPF models (Figure 7b) is apparent at a wavelength of 0.7 μm. (c) Similar comparison for the model surface albedo, where the effective TES solar band weighting for surface rather than atmospheric scattering is indicated by the dash-dotted line. Agreement between the equivalent EPF models (Figure 7b) is apparent at ~0.7 μm.

solutions constructed from wavelength-resolved modeling of the TES solar band channel show excellent agreement with wavelength-independent EPF solutions at a wavelength of ~0.7 μm. Resolved wavelength-solar band agreement at 0.7 μm is valid for EPF solutions of aerosol extinction optical depth, single scattering albedo, and surface albedo.

2.4. Model-Data Comparisons

[22] The TES EPF sequences presented in Figures 2–5 each include three best-fit RT simulations (distinguished by the various line types), corresponding to three adopted models of the aerosol single scattering behavior. While the fitted reflectances are represented by continuous lines for visual clarity, model reflectances are actually calculated for a limited set of discrete emission angles found in the observed EPF sequence (specifically; 5 angles for Figure 2, 9 angles for Figures 4 and 5, and 18 angles for Figure 3). The three RT models provided in each figure represent optimal fits for values of the solar band aerosol optical depth and surface albedo, which are indicated on the figures for each of the modeled aerosol types. The several aerosol types adopted for these fits represent a small set of dust and ice single scattering phase functions found to provide reasonable fits to the full range of TES EPF sequences analyzed (~350). An aerosol single scattering albedo (ssa) is adopted for each of the model aerosol single scattering phase functions, as consistent with a dust versus ice composition (based on the scattering phase function and the coincidentally measured thermal IR spectrum) and dust EPF sequences observed during the 2001 global dust storm (see below). Two of the derived dust single scattering phase functions presented in Figures 2 and 3 are equivalent to dust scattering phase functions retrieved by previous Pathfinder [*Tomasko et al.*, 1999] and Viking IRTM EPF [*Clancy and Lee*, 1991] analyses. However, the two types of ice scattering phase functions (Figures 4 and 5) are unique results of the current analysis. Both the dust and ice angular scattering behaviors are developed and discussed in detail in following sections. Here, we demonstrate the degree of specificity provided by RT model fits to the TES EPF sequences over a representative range of observing and Mars atmospheric aerosol conditions.

[23] Several important aspects of model RT fits to the EPF sequences are displayed in Figures 2–5, which lead to the following characterizations. Firstly, low emission angle brightnesses are more sensitive to the surface albedo and the higher emission angle brightnesses to the aerosol optical depth. The directness of this relationship is modified by

variable conditions such as the surface albedo and incidence angle, and the magnitude and type of aerosols present. Secondly, the goodness of fit obtained for most (but not all, see Figure 3) EPF sequences is strongly affected by the aerosol single scattering phase function, indicating that TES EPF sequences provide significant constraints on aerosol types. Figures 4 and 5 illustrate the distinction in best-fits between two primary ice aerosol types, Figure 2 indicates modest discrimination for variations in the dust scattering phase function. Finally, derived solar band optical depths and surface albedos are only modestly sensitive to the aerosol single scattering phase function and albedo, for low-to-moderate aerosol loading. This condition changes significantly for aerosol optical depths >1, such as during the 2001 planet-encircling dust storm. EPF model-data comparisons for this regime are presented in a later section.

3. Results

3.1. Phase Functions and IR Spectra of Aerosol Types

[24] On the basis of monochromatic fits to roughly 350 separate TES solar band EPF sequences (roughly 1% of the total observed by late 2002), we derive the coarse latitudinal and seasonal (L_S) variations of dust and ice aerosol scattering properties at an equivalent wavelength of 0.7 μm, as demonstrated above. The selected EPF sequences provide optimized (roughly contiguous) sampling in latitude and L_S over the 45°S and 45°N latitude range for which full seasonal coverage is obtained. We have further categorized the dust and ice cloud scattering properties on the basis of coincident TES thermal IR spectra and solar band/thermal infrared optical depths derived for a subset of the analyzed solar band EPF sequences. Figure 10 presents the derived set of aerosol single scattering phase functions, consisting of three primary types (dust, seasonal ice-type 1, and aphelion ice-type 2), and a secondary dust type (bright dust) we associate with dust aerosols overlain by optically thin, high-altitude ice (type 1) clouds. Two phase functions are derived for each of the ice and dust aerosol types, to accommodate the observed degree of variation in scattering required to fit the full range of EPF sequences analyzed. The less backscattering of the two dust types compares directly to the Pathfinder dust scattering phase function derived by *Tomasko et al.* [1999], and the more backscattering case is equivalent (for phase angles <160°) to the IRTM EPF dust scattering phase function derived by *Clancy and Lee* [1991]. The range of scattering variations observed among the type 1 and type 2 ice aerosols appears most significant at side scattering phase angles (70–120°).

[25] The symbols of the aerosol types displayed in Figure 10 are maintained throughout this paper to represent their spatial, seasonal, and spectral behaviors throughout this paper for consistency and visual clarity. Where practical, we also adopt consistent colors for each aerosol type to aid distinction. The range of phase angles presented in Figure 10 indicates the full range of observational coverage for the complete data set, whereas individual EPF sequences typically extend over 60–80° of phase angle variation. The forward scattering peak (phase angle = 160–180°) is not directly constrained by this analysis. Consequently, we have adopted the Pathfinder [*Tomasko et al.*, 1999] dust phase function shape in this scattering regime, properly normalized for each of the aerosol phase functions displayed in Figure 10. Because the single scattering asymmetry parameter (g) is strongly dependent on the details of the forward scattering peak (e.g., for phase angles ≥170°), our EPF analyses are not well suited to measurement of this parameter. However, for reference, values of g for the single scattering phase functions of dust, type 1, and type 2 ice aerosols as presented in Figure 10 are 0.64–0.67, 0.62–0.63, and 0.66–0.68, respectively.

[26] Modeling studies of aerosol particle shapes, based on T-matrix and finite-element algorithms, using the observed phase functions of Figure 10, provide as yet preliminary conclusions regarding the distinct physical characters of these ice and dust aerosols [e.g., *Wolff et al.*, 2000]. The relatively narrow minimum in scattering at 80–100° phase angles exhibited by type 2 ice particles appears most consistent with nonangular, spheroidal particle shapes. By comparison, the absence of a distinct side scattering minimum coupled with the presence of a sharp rise in the backscattering (20–40° phase angles) for type 1 ice aerosols suggest crystalline shapes. The precise crystalline geometry is not yet determined, but possible candidates include an octahedral shape as might be expected for the Ice 1c crystalline state. The relatively constant side-to-back scattering cross section observed for Mars dust is reasonably well modeled by disk particle shapes with moderate axial ratios (0.5–2.0), such as presented by *Mishchenko et al.* [1997].

[27] Figure 11 presents a comparison of the basic IR spectral behaviors for the aerosol types as categorized by their scattering phase functions in Figure 10. The two aerosol ice types display distinctly different IR spectral shapes, apparently reflecting a bimodal size distribution for Mars ice clouds. The small type 1 ice clouds (green spectrum in Figure 11) present peak 12 μm absorption shortward of the 15 μm CO_2 band, and generally weak ice absorption longward at 18–20 and 30–40 μm. In contrast, the larger type 2 ice clouds (blue spectrum in Figure 11) exhibit peak 12 μm absorption extending into the CO_2 15 μm band, as well as significant absorptions at 18–20 and 35–40 μm. A single dust spectrum is included in Figure 11 (red spectrum), indicating the well known 9 μm and 18–22 μm absorption structure of Mars dust [e.g., *Toon et al.*, 1977]. The relative strengths of these two dust absorption bands are affected by the dust particle size distribution [see *Wolff and Clancy*, 2003]. We show a single dust spectrum in Figure 11 because although dust aerosols present significant particle size variations, we have not identified separate dust types as distinctive as the type 1 and type 2 ice aerosol populations. For example, the bright dust scattering phase function indicated in Figure 10 does not present a correspondingly distinct IR spectral behavior, but rather appears to result from high-altitude, small-particle type 1 ice components which are exhibited weakly, if at all, in the IR spectrum. For cases in which the observed IR spectrum and solar band/thermal IR optical depth ratios indicate unusually large dust particle sizes ($r_{eff} \geq 1.8$ μm, see following), a distinctive change in the dust single scattering phase function is not identified. Of course, larger particle sizes likely result in greater forward scattering, which is beyond the observational constraints provided by TES EPF sequences. Nevertheless, we do

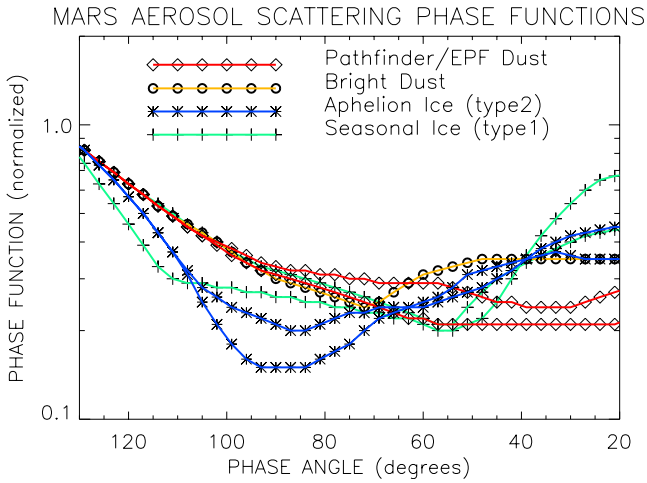

Figure 10. The set of Mars dust and ice aerosol single scattering phase functions found to provide adequate solutions for the full range of ~350 TES solar band EPF sequences fit in this study. The Pathfinder [*Tomasko et al.*, 1999] and Viking IRTM [*Clancy and Lee*, 1991] single scattering phase functions for Mars dust aerosols (lower and upper red-diamond lines, respectively) fit the range of dust-only scattering conditions modeled. The bright dust model (yellow- circle line) corresponds to predominantly dust scattering cases where unresolved (in the thermal IR) ice aerosols appear to contribute increased backscattering. The seasonal ice phase functions (green-plus lines) indicate the range of phase scattering exhibited by type 1 ice aerosols. The aphelion ice phase functions (blue-asterisk lines) indicate the range of phase scattering exhibited by type 2 ice aerosols.

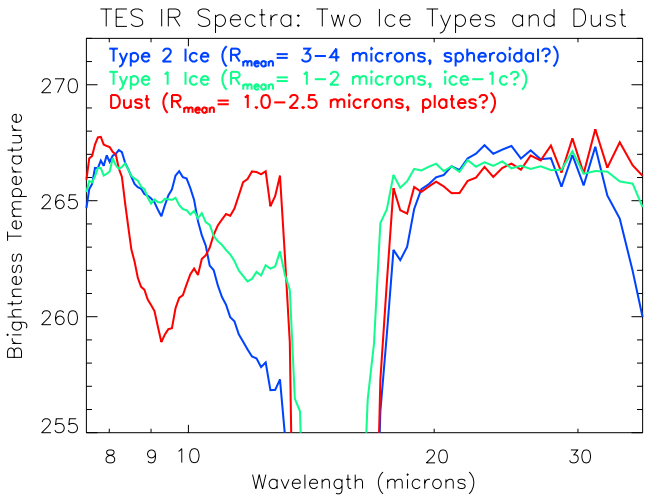

Figure 11. Representative TES thermal IR spectra corresponding to the Mars dust (red line) and two ice aerosol types (type 1- green line, type 2- blue line) categorized by their visible scattering phase functions in Figure 10. Type 2 ice clouds are generally of higher optical depth than type 1 ice clouds, and exhibit deeper long wavelength absorptions (at 18 and 40 μm). The smallest particle sizes observed for type 1 ice aerosols (r_{eff} = 1 μm) exhibit 12 μm absorptions which peak distinctly shortward of the deep 15 μm absorption band contributed by atmospheric CO_2. The mean particle size ranges and shapes indicated for these aerosol types are discussed in the text.

not see distinguishing changes in the observed side and backscattering behaviors of these larger particle size dust populations, as we do for type 1 versus type 2 ice populations.

3.2. Distribution of Aerosol Types and Optical Depths

[28] Figure 12 presents visible (solar band) optical depths and aerosol types from roughly 350 TES EPFs analyzed, as a function of Mars latitude (45°S–45°N) and L_S (0–360°). The colored symbols denote individual EPF measurements by aerosol type; blue asterisk symbols for type 2 aphelion ice aerosols, green plus symbols for type 1 seasonal ice aerosols, red diamond symbols for dust aerosols, and brown circle symbols for bright dust aerosols (presumably dust with a high-altitude type 1 ice component). The shaded contour levels present the total visible aerosol optical depth, as derived from a smoothed, interpolated fit to the coarse latitude-L_S grid of analyzed values (i.e., the colored symbols). As apparent from the distribution of plotted symbols, TES coverage is most complete at intervals of 15° latitude, with limited coverage at intervals of 7.5° latitude (e.g., ±7.5, 22.5, and 37.5°). The range of L_S coverage presented in Figure 12 begins at L_S = 100° in 1999 and extends through L_S = 140° in 2001. Consequently,

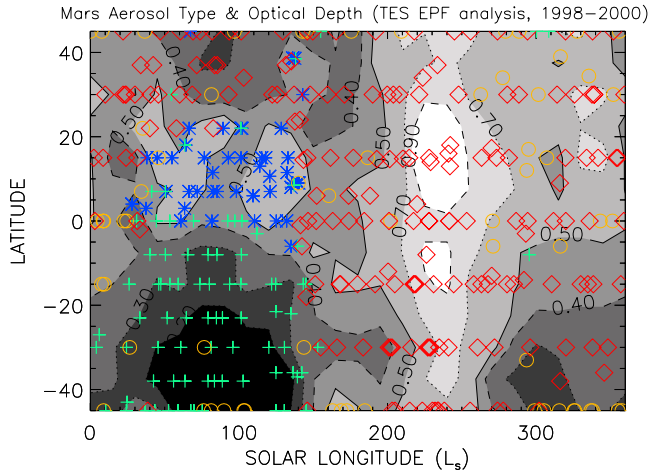

Figure 12. Shaded contour plot of Mars total aerosol extinction optical depth versus Mars season (L_S) and latitude (45°S–45°N), for the 1998–2000 period of MGS mapping operations. These aerosol optical depths are derived from ~350 TES solar band EPF fits, for which the effective wavelength of measurement is 0.7 μm. The colored symbols represent locations of individually analyzed EPF sequences, where the symbol shape and color designate the dominate aerosol type as determined from the solar band scattering phase dependence and the thermal IR absorption spectrum. Peak dust (red diamonds) optical depths of 1.0–1.2 are present within the white shaded region at L_S = 220°, corresponding to regional dust storm activity observed in 1999 [see *Smith et al.*, 2000]. Minimum optical depths of ≤0.1 occur at L_S = 30–110° in the southern hemisphere, composed largely of type 1 ice clouds (green plus symbols). Type 2 ice clouds (blue asterisk symbols) are restricted to northern subtropical, L_S = 30–140° occurrence of the aphelion cloud belt.

the July 2001 global dust storm, beginning at L_S = 185°, is not represented in this figure. The presented range corresponds to portions of two Mars years (years 24, 25 from 1955, as defined by *Clancy et al.* [2000]) which were very similar in behavior, as indicated by *Smith et al.* [2001].

[29] Several aspects of Mars aerosol behavior are apparent in Figure 12. In particular, the orbital variation of ice versus dust aerosols is very distinct. Ice clouds dominate at the largest Sun-Mars distances (L_S = 20–140°). The abrupt disappearance of wide-scale (i.e., nontopographic) ice clouds occurs at L_S = 140–145°, a behavior repeated in the first two Mars years (24,25) observed by MGS. This behavior also occurs much earlier in season than the global increases in dust loading associated with the approach of perihelion and southern summer (i.e., shortly after L_S = 200° in 1999, and L_S = 185 in 2001). Secondly, the distributions of the two types of ice cloud aerosols are also very distinct from one another. Type 1 ice clouds (green plus symbol) are most prominent in the southern hemisphere winter (L_S = 20–140°), but also correspond to higher latitude and topographic ice clouds at all L_S values. Type 2 ice clouds (blue asterisk symbols) are restricted to the aphelion period (L_S = 20–140°) and the equatorial to northern subtropical latitudes (0–30°N). This temporal and spatial distribution of the type 2 ice coincides with the aphelion cloud belt structure, as first described and associated with the northern summer Hadley circulation by *Clancy et al.* [1996].

[30] In terms of the latitudinal and L_S distributions of aerosol (ice + dust) optical depths, the most basic features are larger aerosol columns in the northern versus the southern hemisphere (by ~factor of two), and over the L_S range of 200–360° versus 0–200° (also by ~factor of two). The north-south optical depth gradient is largely a consequence of the north-south gradient in surface elevation, or surface pressure. A correspondence of optical depth with surface pressure results for the case of constant dust concentrations (or mixing ratios), as forced by the strong meridional circulation of the Mars atmosphere. This effect does not strictly explain the asymmetric north-south distribution of aerosol optical depths in the L_S = 20–140° aphelion period, which is affected by increased water ice clouds over the ascending Hadley branch at 0–30°N latitudes in this northern summer season. The primary orbital variation (L_S) in the total aerosol optical depth is dominated by increased dust loading during the perihelion period, due to regional dust storm activity at L_S ~ 220° in 1997 and 1999 [*Christensen et al.*, 1998; *Smith et al.*, 2000]. The global dust storm beginning at L_S = 185° in 2001 is not shown in Figure 12. Also significant is a modest increase in global dust optical depth at L_S = 320° an event which occurred with remarkable similarity in all three of the Mars years observed by MGS (M. Smith, personal communication, 2002).

[31] In general, the magnitude and distributions of visible aerosol optical depths indicated in Figure 12 compare well with TES thermal infrared total optical depths (dust at 9 μm and ice at 12 μm [e.g., *Smith et al.*, 2000]) scaled by a factor of two. This scaling corresponds to typical visible-to-infrared optical depth ratios of 0.5 for 1.5–2.0 μm radii dust particles [*Zurek*, 1982; *Clancy et al.*, 1995], which we find to be a common size range for Mars dust aerosols. In addition, this scaling is approximately correct for the high-end size range for type 1 and low-end size range for type 2 ice aerosols (see below). However, there are three specific conditions in which the derived visible aerosol optical depth does not scale as roughly twice the thermal infrared optical depth. Higher visible-to-infrared optical depth ratios (~3) are found for the smaller type 1 ice particles, and for dust aerosols within the 70–200° and 320–340° L_S range at northern latitudes. In addition, the larger type 2 ice particles yield lower visible-to-infrared optical depth ratios (approaching 1). Consequently, the northern hemisphere over L_S = 20–200° shows noticeable departures from thermal infrared optical depths simply scaled by a factor of two. We also point out that we have not scaled the visible optical depths presented in Figure 12 with surface pressure (i.e., topography), as is commonly done for TES thermal infrared presentations [e.g., *Christensen et al.*, 1998; *Smith et al.*, 2000].

3.3. Dust and Ice Aerosol Particle Sizes

[32] In addition to providing visible scattering properties and optical depths, the TES solar band EPFs yield accurate measurements of aerosol particle sizes when combined with TES thermal infrared optical depth determinations. Generally, the wavelength variation of an aerosol extinction cross section is most diagnostic for comparisons between wavelengths several times larger than the mean particle size and wavelengths comparable to or several times smaller than the mean particle size of the aerosol size distribution. For the case of Mars, observed optical depth ratios from simultaneous thermal IR and visible measurements can provide reasonably accurate (~10%) determinations of dust and ice aerosol sizes over a 0.5–5 μm range of particle radii. However, it is important to recognize the very different proportions of scattering and absorption that contribute to the total extinction optical depths retrieved for Mars dust/ice aerosols at visible versus thermal IR observing wavelengths. Aerosol extinction at visible-to-near IR wavelengths is contributed primarily by scattering (ssa $\geq$ 0.94), whereas thermal IR extinction is dominated by absorption (particularly within the 9 μm dust and 12 μm ice features, where ssa $\leq$ 0.5). Consequently, thermal IR optical depths are much larger relative to visible optical depths for Mars aerosols (IR-to-visible ratios $\geq$ 0.3) than would be presented by scattering-only extinction (IR-to-visible ratios $\leq$ 0.05). The particle size information also becomes modestly dependent on the IR dust and ice optical properties (real and imaginary indices of refraction) employed to compare observed and modeled optical depth ratios. This is not a problem for ice aerosols, for which optical indices can be adopted from accurate laboratory measurements. It is somewhat more problematic for the unknown dust optical properties, although such modeling errors prove to be less significant than the absolute retrieval errors associated with the optical depth determinations in the solar band and thermal IR from TES observations.

[33] Figure 13 presents the modeled variation of dust optical depth ratios for solar band (visible-to-near IR)/thermal IR (9 μm) as a function of visible-to-near IR wavelength (horizontal axis, 0.3 to 4.0 μm) and dust aerosol particle size (various line types). The adopted thermal IR

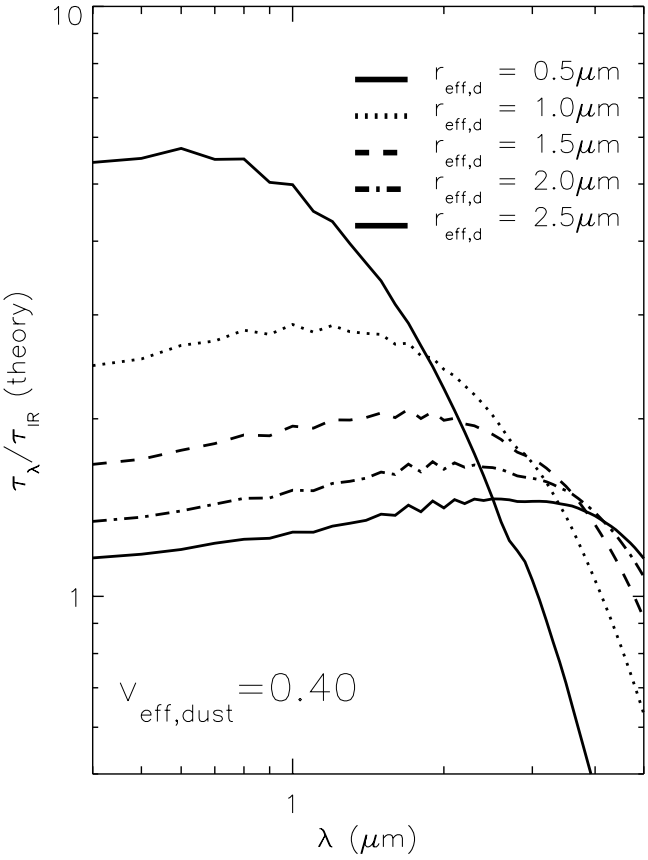

Figure 13. Mie calculations of the ratio of dust extinction optical depth, as a function of wavelength, to the dust extinction optical dust at a wavelength of 9 μm (1075 cm^{-1}, beyond the right-hand extent of this plot). At solar band wavelengths (λ = 0.4–1.2 μm), this ratio is strongly dependent on the dust particle size, as indicated by the model range of particle sizes presented by the various line types (r_{eff} = 0.5–2.5 μm). These ratios are weakly dependent on the assumed width of the dust size distribution (v_{eff} = 0.4 for the presented cases).

optical properties for the dust model are described by *Wolff and Clancy* [2003], and the solar band optical properties are based on a palagonite model as described by *Clancy et al.* [1995]. The five particle size models presented in Figure 13 correspond to a range of average effective (extinction cross-section weighted) dust particle radii (r_{eff}) employing a modified gamma size distribution [from *Deirmidjian*, 1964] with a size variance of 0.4 μm (as adopted by *Toon et al.* [1977] and *Clancy et al.* [1995]). Notice that the wavelength variation of visible-to-near IR/9 μm optical depth ratio is relatively modest across the solar band pass, especially as compared to its variation with effective aerosol particle sizes typical of Mars dust aerosols ($r_{eff} \sim$ 0.5–3.0 μm). Similarly, Figure 14 presents the modeled variation of visible-to-near IR/12 μm optical depth ratios for water ice aerosols as a function of the visible-to-near IR wavelength (horizontal axis, 0.3 to 4.0 μm) and ice aerosol particle size (various line types). Ice optical indices are adopted from *Warren* [1984] and a much narrower particle size variance (0.1 μm) is used for the various model particle sizes (1 to 6 μm). Such narrow size distributions follow predictions from ice particle microphysics [e.g., *Michelangeli et al.*, 1993] and are consistent with the Mariner 9 IRIS analysis of *Curran et al.* [1973]. Values of particle size variance within factors-of-two of those adopted in Figures 13 and 14 do not dramatically change the model solar band/thermal IR optical depth ratios for either dust or ice aerosols. However, *Glenar et al.* [2003] have recently analyzed near IR spectroscopic images of the 1999 apehlion cloud belt at L_S = 130° in terms of very broad ice particle size distributions, which we have not considered.

3.3.1. Comparisons to Smith et al. IR Optical Depths

[34] Our most accurate determinations of solar band/IR optical depth ratios employ independent thermal IR spectral retrievals of particle size and optical depth, as described by *Wolff and Clancy* [2003]. These thermal IR optical depths are more accurate than the standard GSFC aerosol optical depth retrievals [*Smith et al.*, 2000] in that aerosol scattering is incorporated in the radiative transfer. This also provides for self-consistent retrieval of the total IR extinction optical

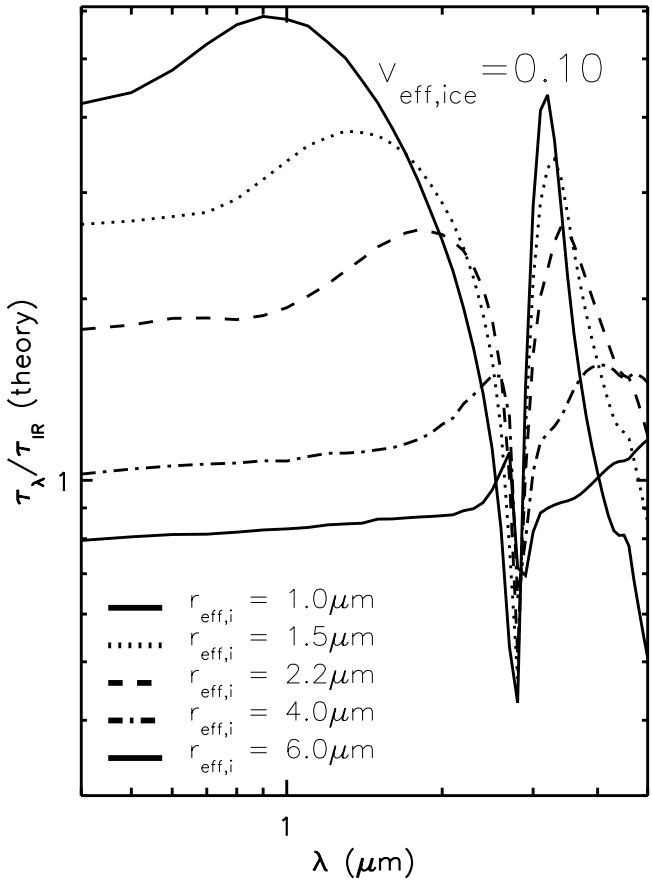

Figure 14. Mie calculations of the ratio of water ice extinction optical depth, as a function of wavelength, to the ice extinction optical dust at a wavelength of 12 μm (825 cm^{-1}, beyond the right-hand extent of this plot). At solar band wavelengths (λ = 0.4–1.2 μm), this ratio is strongly dependent on the ice particle size, as indicated by the model range of particle sizes presented by the various line types (r_{eff} = 1–6 μm). These ratios are weakly dependent on the assumed width of the ice size distribution (v_{eff} = 0.1 for the presented cases).

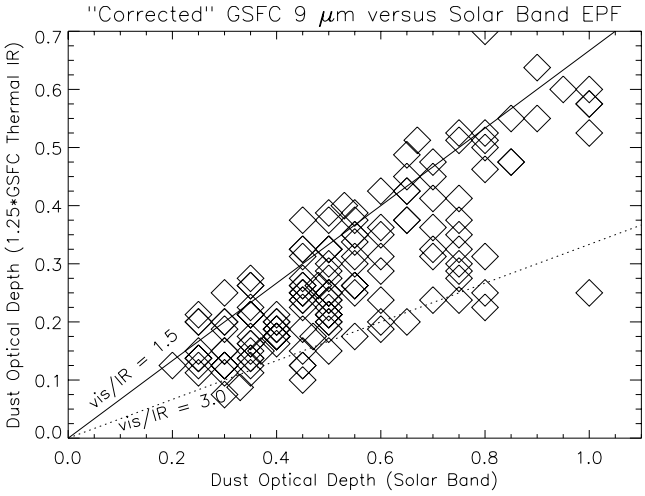

Figure 15. Dust optical depths in the 9 μm absorption band (from the Goddard Space Flight Center TES atmospheric database [*Smith et al.*, 2000]) are plotted versus their corresponding TES solar band optical depths. The 9 μm optical depths have been scaled by a factor of 1.25 to account for neglect of dust scattering effects and optical depths in the GSFC optical depth retrievals [see *Wolff and Clancy*, 2003]. Approximate bounds in resulting solar band-to-thermal IR dust optical depth ratios of 1.5 (solid line) and 3.0 (dotted line) are indicated. At higher dust optical depths ($\tau_{solar\ band} \geq 0.8$), observed ratios ≥ 2 become noticeably absent.

depth, versus the absorption optical depth provided by the GSFC retrievals. Consequently, *Wolff and Clancy* [2003] aerosol optical depths are generally 25–30% larger than GSFC IR optical depth values. Full scattering calculations also allow self-consistent analysis of aerosol particle sizes based on the thermal IR variation of aerosol optical depth (e.g., 9 versus 20 μm for dust). However, we have far fewer thermal IR spectral fits (∼50) than TES solar band EPF fits (∼350). Comparison of all TES solar band optical depths with corresponding thermal IR aerosol optical depths from the standard TES atmospheric data base (9 and 12 μm optical depth retrievals [*Smith et al.*, 2001] provides better resolution of the seasonal and latitudinal variations in the solar band/IR optical depth ratios for Mars dust and ice aerosols. Figure 15 presents a scatter plot of GSFC thermal IR versus EPF solar band optical depths for "dust" aerosols only. The GSFC optical depths are scaled by a factor of 1.25 as an approximate correction for the neglect of infrared scattering effects in these retrievals: i.e., GSFC values are measurements of absorption-only optical depths. We have also arbitrarily defined "dust" conditions as measurements for which the GSFC 9 μm optical depth is more than 3 times the GSFC 12 μm ice optical depth, and for which the GSFC 12 μm ice optical depth is less than 0.10. These plotted "dust" optical depths are actually the sum of the 9 μm dust and 12 μm ice GSFC optical depths. This accounts for the fact that the solar band optical depth implicitly includes any ice aerosol present, however limited by our GSFC 12 μm selection criteria it may be.

[35] In general, the EPF solar band and GSFC thermal IR optical depths correlate well, given the substantial error bars associated with individual measurements (as plotted for several representative points). The sparseness of high optical depths in this figure is indicative of the relatively modest dust storm activity during the perihelion season of 1998–1999 (we present a few high optical depth measurements obtained during the 2001 global dust storm in a later section). The solid and dashed lines of Figure 15 bound the observed spread in solar band/thermal IR optical depth ratios, from 1.5 (solid line) to 3.0 (dashed line). A value of 1.7 is the approximate ratio expected for a mean dust particle radius of 1.6 μm, roughly consistent with previous Pathfinder [*Tomasko et al.*, 1999] and Viking [*Clancy et al.*, 1995] analyses. The lower bound ratio of 3 (dashed line) corresponds to mean dust particles radii as small as 0.9 μm (Figure 13). A striking feature of the optical depth ratios apparent in Figure 15 is that values significantly higher than 2 become noticeably absent for high dust loading conditions (e.g., solar band optical depth ≥ 0.8). Figure 16 indicates that the low-to-moderate dust loading conditions which exhibit anomalously high solar band/thermal IR optical depth ratios are especially prevalent during the northern summer season ($L_S = 70–200°$), and show a rapid transition to nominal optical depth ratios (∼1.7) shortly after $L_S = 200°$. High solar band/thermal IR optical depth ratios also appear sporadically about $L_S = 320–340°$. As we discuss in a following section, such high solar band/thermal IR optical depth ratios indicate distinctly smaller dust particle sizes which are most prevalent in the northern hemisphere, with the seasonal characters displayed in Figure 16.

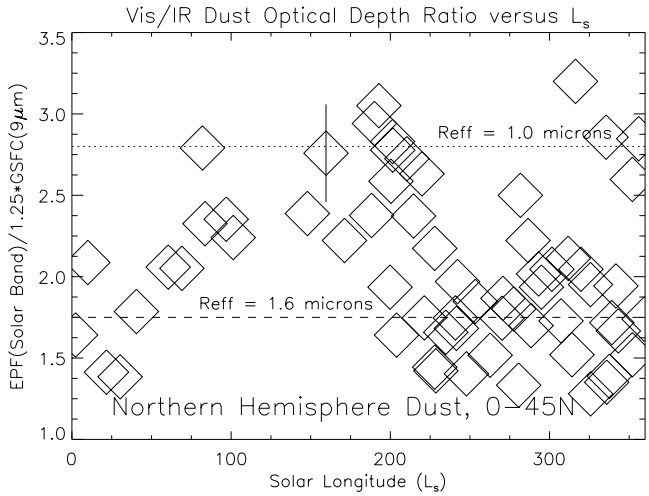

Figure 16. Dust optical depth ratios, calculated from TES solar band (current analysis) and 9 μm absorption band (GSFC [*Smith et al.*, 2000]) retrievals, are plotted versus L_S. The 9 μm optical depths have been scaled by a factor of 1.25 to account for neglect of dust scattering effects and optical depths in the GSFC optical depth retrievals [see *Wolff and Clancy*, 2003]. This comparison is limited to northern hemisphere measurements and for conditions of minimal ice content, which reduces the number of comparisons in the aphelion period considerably. Dashed and dotted horizontal lines indicate the predicted optical depth ratios for dust mean particle radii of 1.6 and 1.0 μm, respectively. An abrupt transition from smaller to larger dust particle sizes is apparent at an L_S of 200°.

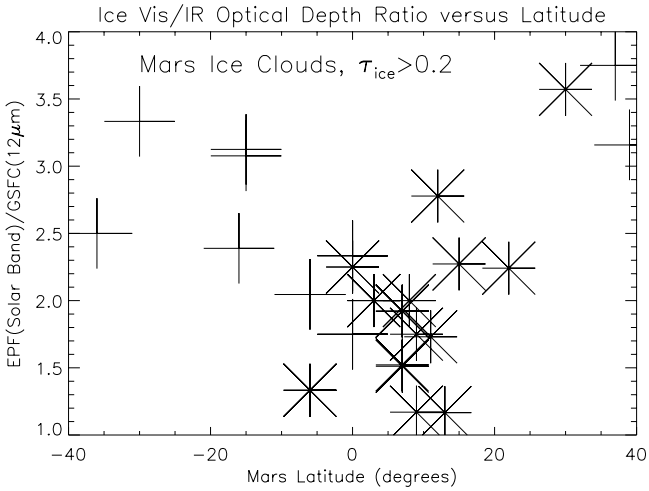

Figure 17. Ice optical depth ratios, calculated from TES solar band (current analysis) and 12 μm absorption band (GSFC [*Smith et al.*, 2000]) retrievals, are plotted versus latitude. This comparison is limited to conditions in which the solar band ice optical depth exceeds 0.2, which generally corresponds to aphelion cloud belt conditions. Type 2 ice aerosols (asterisk symbols) exhibit smaller optical depth ratios, relative to type 1 ice aerosols (plus symbols), indicating larger particle sizes for ice aerosols within the northern subtropical aphelion cloud belt.

[36] Figure 17 presents the latitudinal dependence of solar band/thermal IR optical depth ratios for "ice" aerosols, selected for cases in which the GSFC 12 μm optical depth is greater than 0.2. This effectively selects for northern spring-summer conditions (L_S = 0–140°), when high ice optical depths are present at low northern latitudes. Similar to Figure 16, the thermal IR "ice" optical depths of this figure are combined 12 and 9 μm optical depths from the GSFC data base. The most notable feature of this plot is a significant minimum in solar band/thermal IR optical depth ratios over the 10°S–20°N latitude range, corresponding to the aphelion cloud belt position [*Clancy et al.*, 1996]. The distribution of the plotted asterisk symbols indicate that minimum ratios are primarily populated by type 2 ice clouds, as identified by their distinctive scattering phase functions. Ice solar band/thermal IR optical ratios near 1.0 (4.0) are shown to be indicative of 4 (1) μm mean particle radii in the following section.

3.3.2. Comparisons to Wolff and Clancy IR Optical Depths

[37] Figure 18 presents the range of solar band/thermal IR optical depth ratios retrieved for approximately 50 TES EPF sequences that have been analyzed for both solar band and thermal IR (9 and 12 μm) optical depths. As with prior figures, the diamond symbols indicate primarily dust aerosols, the plus symbols indicate primarily type 1 ice aerosols, and the asterisk symbols indicate primarily type 2 ice aerosols. These categories are based on the specific solar band phase function and thermal IR compositional fits, similar to the above GSFC comparisons. However, we have refit all of the solar band EPF sequences represented in Figure 18 as two-component models in which the proportions of dust and ice (including their specific phase scattering properties) are specified according to the *Wolff and Clancy* [2003] thermal IR solutions. The corresponding effective particle radius for each EPF measurement is then calculated self-consistently on the basis of the adopted visible-through-thermal IR dust and ice optical models, as presented in Figures 13 and 14. The offset in particle size dependence between the ice and dust solutions is a consequence of the distinct optical indices for water and silicate compositions. A roughly linear dependence of particle size with optical depth ratio for both cases reflects the logarithmic scaling of the plot. The smoothness of this dependence does not reflect the considerable uncertainties associated with the retrieved optical depth ratios, which are indicated in subsequent figures. Nevertheless, Figure 18 provides as self-consistent a presentation of Mars optical depth ratios versus particle size as is currently possible.

[38] In Figures 19 and 20, we compare dust and ice particle sizes as derived from the optical depths ratios of Figure 18 (horizontal axis) and from the thermal IR spectral fitting analysis of Wolff and Clancy (vertical axis). There are clearly significant variations in both dust and ice aerosol particle sizes, corresponding to specific seasonal and latitudinal behaviors. Prior to the 2001 global dust storm, the average dust particle radius (r_{eff}) was 1.5 μm, with much smaller dust particle sizes (r_{eff} = 0.8–1.2 μm) implied by large solar band/thermal IR optical depth ratios during the L_S = 70–200° and 320–340° periods (corresponding to peak values for the solar band/thermal IR optical depths ratios in Figure 17). However, significantly larger values for

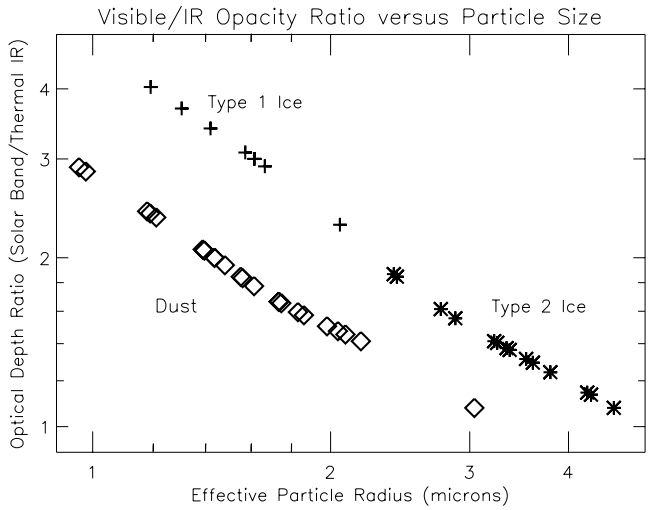

Figure 18. Approximately 30 values of solar band to thermal IR aerosol optical depth ratios are determined, employing 9 and 12 μm dust and ice optical depths from the full RT scattering analysis of TES spectra by *Wolff and Clancy* [2003]. These more accurate aerosol optical depth ratios are presented on the vertical axis versus the implied aerosol particle size, r_{eff}, as calculated from the Mie dust and ice optical depth-particle size dependences of Figures 13 and 14, respectively. Dust particles (diamond symbols) exhibit a range of r_{eff} between 1 and 3 μm, type 1 ice particles (plus symbols) a range of r_{eff} between 1 and 2 μm, and type 2 ice particles (asterisk symbols) a range of r_{eff} between 2.5 and 4.5 μm.

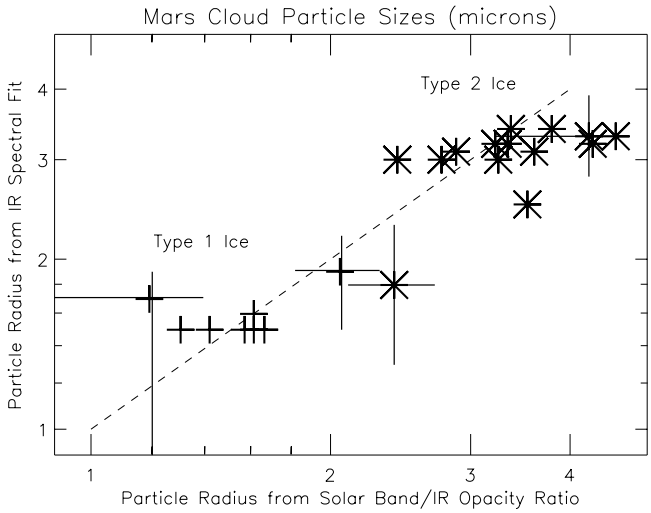

Figure 19. Cross comparison of two distinct methods of particle size measurement for Mars ice aerosols. Particle size determinations based on the solar band to thermal IR optical depth ratios from Figure 18 are presented on the horizontal axis. Ice particle sizes determined from the relative depths of 12 and 18 μm ice absorptions [*Wolff and Clancy*, 2003] are presented on the vertical axis. As indicated by representative error bars, the solar band to IR optical depth ratio becomes less sensitive at large particle sizes, and the thermal IR absorption depth ratio less sensitive at small particle sizes. Taken together, the two techniques retrieve values of r_{eff} between 1 and 2.5 μm for type 1 ice particles (plus symbols), and r_{eff} between 2.5 and 4 μm type 2 ice particles (asterisk symbols).

the cross section weighted mean dust particle radius (r_{eff} = 1.8–2.5 μm, as determined by both methods) were observed in the southern hemisphere during the peak of the 2001 global dust storm. Ice aerosol particle sizes exhibit a larger range of r_{eff} = 1–4 μm particle radii, corresponding to two distinct cloud populations. The smallest ice particle sizes (r_{eff} = 1.0–1.5 μm) are presented by the type 1 ice aerosols, prominent over the southern hemisphere during L_S = 0–140° and as clouds formed over the largest volcanoes in all seasons. The largest ice particle sizes (r_{eff} = 3–4 μm) are exhibited within the aphelion cloud belt between latitudes of 10°S to 30°N for the L_S range of 30–140°.

[39] Within their distinctive uncertainties, the two methods of aerosol particle size determination provide equivalent results, as indicated by the dashed diagonal lines in Figures 19 and 20. Agreement is well defined at intermediate particle sizes (r_{eff} = 1.4–2.4 μm), where accuracies for both methods are optimum. Correlation between the two methods degrades at small particle sizes (r_{eff} = 1–1.5 μm), where infrared spectral fits become insensitive to aerosol particle size; and at large particle sizes ($r_{eff} \geq 3$ μm), where visible/IR optical depth ratios become asymptotic and high optical depth effects more problematic. The latter issue is a particularly significant limitation during the 2001 global dust storm, when the largest dust particle sizes are observed. Consequently, small dust and ice particle sizes are well determined only by visible/IR optical depth ratio determinations, and large particle sizes are most reliably obtained by the IR spectral fitting method.

[40] Taken together, these highly complementary determinations of Mars aerosol particle sizes yield a self-consistent description of seasonally dependent cloud and dust particle size variations. Seasonal type 1 ice aerosols exhibit small particle sizes (r_{eff} = 1–2 μm), where the upper end of this size range corresponds to the ~2 μm ice aerosols identified by *Curran et al.* [1973] and *Pearl et al.* [2001] for two water ice clouds over volcanic features. The aphelion, type 2 ice aerosols exhibit larger particle sizes (r_{eff} = 3–4 μm). There are significant variations in ice cloud particle sizes among the observed ice clouds for each type, and the transition between the two types is not well defined at intermediate particle sizes (r_{eff} = 2–3 μm). It is possible that the two ice types coexist at the boundaries of the aphelion cloud belt (Figure 12), or that the microphysical transition from type 1 ice to type 2 ice is fairly continuous. The limited spatial-seasonal resolution of the present study is not adequate to resolve this question. In addition, cloud particle sizes are very likely to exhibit significant vertical dependences, which are also unresolved in this study. On the basis of near IR spectral absorption shapes, *Glenar et al.* [2003] argue that the particle size distribution of the aphelion cloud belt is very broad, possibly due to vertically dependent size variations. We do note that our current analysis does not indicate a dependence of retrieved ice particle size versus surface elevation (i.e., longitude) within the aphelion cloud belt, but the coarse spatial coverage of size retrievals limits the strength of this conclusion.

[41] The most commonly observed dust particle size is found to be 1.5 ± 0.1 μm, consistent with current results from Viking [*Clancy et al.*, 1995; *Pollack et al.*, 1995],

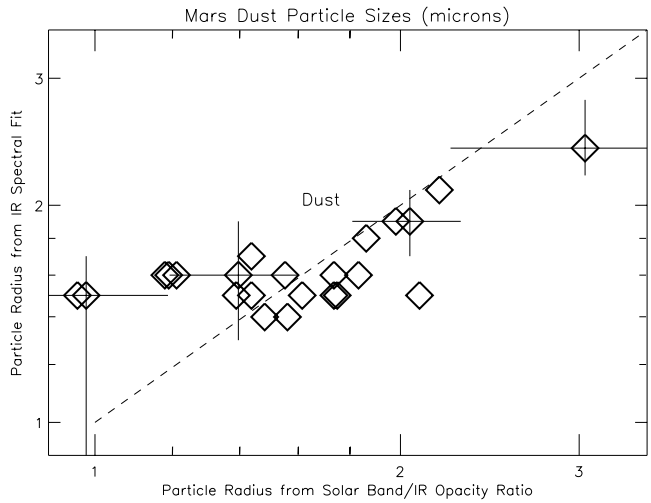

Figure 20. Cross comparison of two distinct methods of particle size measurement for Mars dust aerosols. Particle size determinations upon solar band to thermal IR optical depth ratios from Figure 18 are presented on the horizontal axis. Dust particle sizes determined from the relative depths of 9 and 20 μm dust absorptions [*Wolff and Clancy*, 2003] are presented on the vertical axis. As indicated by representative error bars, the solar band to IR optical depth ratio becomes less sensitive at large particle sizes, and the thermal IR absorption depth ratio less sensitive at small particle sizes. Taken together, the two techniques retrieve values of r_{eff} between 1 and 2.5 μm for dust aerosols.

Pathfinder [e.g., *Tomasko et al.*, 1999] and MGS [*Pearl et al.*, 2001] analyses. However, dust particle sizes clearly exhibit seasonal correlations as distinctive as the ice type association with the aphelion cloud belt. This conclusion is notably different from previous inferences that the dust particle size distribution in the Mars atmosphere is largely invariant, based on agreement between Viking and Pathfinder lander measurements [*Tomasko et al.*, 1999] and Mariner 9 observations of an approximate invariance in the dust IR spectrum (e.g., 9 versus 20 μm [*Toon et al.*, 1977]). The combined sensitivities of the TES solar band EPF and thermal IR spectral retrievals are sufficient to accurately distinguish dust particle size variations and coarsely map their seasonal and spatial dependencies for the first time. In particular, much smaller dust particle sizes (r_{eff} = 1 ± 0.2 μm) are typical for the northern hemisphere during the L_S = 40–200° range, and significantly larger dust particles (r_{eff} = 1.8–2.5 μm) were suspended in the southern hemisphere during the 2001 global dust storm. Once again, the limited spatial-seasonal resolution of this study does not provide a detailed definition of these particle size variations. But it is interesting to note that the seasonal occurrence of small dust particle size over L_S = 40–200° is also suggested by IRTM visible/IR optical depth ratios retrieved from 1977–79 Viking observations [*Martin*, 1986; *Clancy et al.*, 2000; *Toigo and Richardson*, 2000] for this seasonal range. In this case, Viking lander visible optical depths [*Colburn et al.*, 1989] have been compared with contemporaneous IRTM 9 μm optical depths [*Martin*, 1986] to indicate anomalously large visible/IR optical depth ratios during the L_S = 20–200° seasonal range. Although many of the very high ratios calculated for the L_S = 20–140° period are associated with the recently identified aphelion cloud belt [*Clancy et al.*, 1996; *Toigo and Richardson*, 2000], low ratios observed by Viking over the L_S = 140–200° period when the aphelion cloud belt is no longer present remain anomalous [*Clancy et al.*, 2000]. They are, in fact, reasonably consistent with the ratios observed in this season by the current MGS TES study. It should also be noted that visible/IR optical depth ratios determined from Viking IRTM EPF analyses contained instances of large visible/IR optical depth ratios, albeit with large error bars and limited numbers of measurement [*Clancy et al.*, 1995].

3.4. Dust Single Scattering Albedo

[42] The sensitivity of solar band EPF sequences to the aerosol single scattering albedo (ssa) is generally modest except in the case of high dust optical depths (e.g., $\tau \geq 1$). All of our dust EPF fits employ ssa values of 0.92–0.94. Dust EPF fits incorporating the higher ssa value of 0.94 also employ single scattering phase functions in which the backscattering cross section is elevated relative to the *Tomasko et al.* [1999] phase function (see Figure 10). A significant fraction of these brighter dust cases are likely affected by the contribution of low optical depth ice aerosols which are not resolved in the accompanying IR spectra. However, it is possible that finer size populations of Mars dust are indicated in some of these brighter, more backscattering EPF cases. With regard to a more absorbing dust aerosol suggested by early Viking lander analyses (e.g., ssa for solar average weighting = 0.86 [*Pollack et al.*, 1979]), we find that almost all of the TES EPF dust

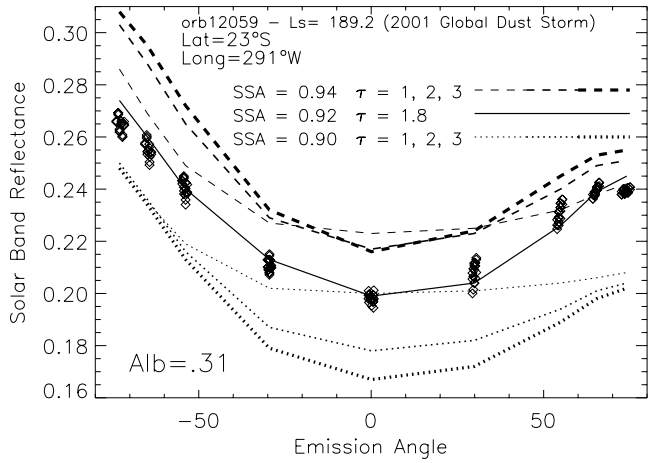

Figure 21. The sensitivity of TES EPF measurements to the dust single scattering albedo (ssa) during high dust loading conditions is indicated by model comparisons to an EPF sequence just north of Hellas Basin at the beginning of the 2001 global dust storm. The best fit model (solid line) to the observations (diamond symbols) employs a visible dust optical depth scaled appropriately from its retrieved 9 μm optical depth (see text) to a value of 1.8, and a best-fit ssa of 0.92. The dashed and dotted curves present model EPF sequences for ssa of 0.94 and 0.90, respectively, for values of dust optical depth at 1, 2, and 3 (increasing line thicknesses for increasing optical depths). The surface albedo is fixed at 0.31 for all of these models, corresponding to a best-fit value for ssa = 0.92.

sequences are poorly fit by ssa $\leq$ 0.90. In the case of higher dust loading conditions, where stronger constraints on the dust ssa apply, the dust ssa is best fit as 0.92–0.93.

[43] Figure 21 compares model EPF reflectance behaviors (lines) for three dust ssa values (0.90, 0.92, and 0.94) to TES solar band EPF observations (diamond symbols) at 23S, 291W shortly after the global expansion of the 2001 planet-encircling dust storm (L_S = 189°). The best-fit model EPF (solid line) is found for a dust ssa value of 0.92 and a surface albedo of 0.31. This assumes a dust visible extinction optical depth of 1.8, which we fix on the basis of the fitted IR spectrum (i.e., a 9 μm optical depth of 1.5 and a mean dust particle size of 2.4 μm [*Wolff and Clancy*, 2003]). In addition, we show the model EPF behaviors for dust single ssa values of 0.90 (dotted lines) and 0.94 (dashed lines) for dust visible optical depths of 1, 2, and 3. The surface albedo is held constant at 0.31 for each of these model cases to demonstrate the trends of EPF reflectances with dust optical depth and dust ssa. For the case of low dust ssa (0.90, dotted lines), increased dust loading darkens the observed reflectance at emission angles less than 50°, and cannot reproduce the observed reflectance at any emission angle $\geq$50°. In fact, only very high surface albedos (Alb $\geq$ 0.38) can reproduce the observed reflectance at the low emission angles. In contrast, high dust ssa values (0.94, dashed lines) can reproduce observed reflectances at low emission angles with significantly lower surface albedos (Alb = 0.14), but will overestimate reflectances at higher emission angles for such surface albedos. Another important point to draw from Figure 21 is the very

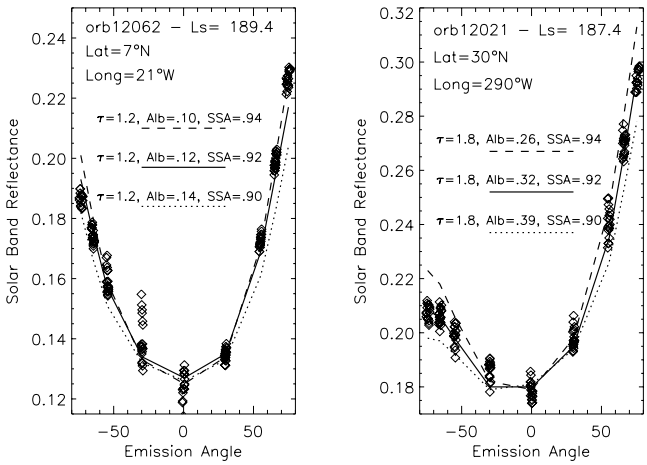

Figure 22. Two additional TES EPF sequences returned during the 2001 global dust storm, indicating the detailed sensitivity of EPF solar band sequences to the dust single scattering albedo (ssa) for high dust optical depths. Best fit models (lines) are compared to the observations (diamond symbols) for ssa of 0.90 (dotted lines), 0.92 (solid lines), and 0.94 (dashed lines). In all cases, the model employs a visible dust optical depth scaled appropriately from its retrieved 9 μm optical depth (see text) to a value of 1.2 in the left panel, and 1.8 in the right panel. The surface albedo (Alb) is varied for each assumption of ssa to obtain a best possible fit to the observations. For both EPF sequences, the best-fit is provided by ssa = 0.92.

different contrast effects of bright (ssa = 0.94) versus dark (ssa = 0.90) dust over bright surface regions on Mars. In particular, dark dust reduces the inferred brightness of bright regions on Mars whereas bright dust is relatively neutral for such regions. In fact, for more typical bright regions on Mars (e.g., $0.20 \geq Alb \leq 0.27$), dust with ssa = 0.92 increases the total (surface and atmosphere) reflectance by 5–10% over pure surface reflectance.

[44] Figure 22 presents best-fit model EPF cases for ssa values of 0.90 (dotted lines), 0.92 (solid lines), and 0.94 (dashed lines) over two additional regions during the 2001 planet-encircling dust storm. The first (left) panel presents EPF models against a TES EPF observation over a dark albedo region (7°N, 21°W), in which solar band dust optical depth is fixed at 1.2, in accordance with the observed TES IR spectrum (i.e., a 9 μm optical depth of 0.7 and a mean dust particle size of 1.8 μm [*Wolff and Clancy*, 2003]). For each of the assumed values for dust ssa, a surface albedo is derived which best fits the observed EPF sequence. For smaller ssa values, higher values of surface albedo are required to reproduce the observed reflectance at low emission angles. At high emission angles, the EPF reflectance is dominated by dust scattering and shows best agreement with ssa model values of 0.92 or 0.94. An ssa value of 0.90 clearly underestimates the observed atmospheric brightness at emission angles greater than 30°. Similarly, the second (right) panel of Figure 22 presents model EPF sequences in comparison to a TES EPF observation over a bright albedo region (30°N, 290°W). Once again, the model solar band dust optical depth is fixed (to 1.8) in accordance with the observed TES IR spectrum (i.e., a 9 μm optical depth of 0.9 and a mean dust particle size of 1.4 μm [*Wolff and Clancy*, 2003]). In this case, the best model-data agreement is obtained for a dust ssa of 0.92. Higher (0.94) and lower (0.90) values for the dust ssa overestimate and underestimate, respectively, the observed EPF reflectances at emission angles greater than 30°. Notice also, that for a dust ssa value of 0.90, an especially high surface albedo (0.39) is required to fit the observed reflectances at low emission angles.

[45] A best-fit solar band average value of $0.92\ ^{+0.2}_{-0.1}$ for the dust ssa is identical to dust ssa values derived from Viking IRTM EPF sequences [*Clancy and Lee*, 1991]. It is also equivalent to the resolved 0.3 to 3.0 μm model of dust ssa presented in Figure 8b, which in turn, provides close agreement with Mars dust ssa values obtained from recent analyses of Mars surface dust reflectance [*Ockert-Bell et al.*, 1997] and Pathfinder atmospheric dust scattering [*Tomasko et al.*, 1999]. For wavelengths longward of 0.6 μm, such high dust ssa values present weak contrast (5–10%) over bright albedo regions on Mars, but can elevate inferred surface reflectances over dark albedo regions by 20–30%. It is also interesting to note that surface albedos derived from such EPF fits indicate significant short-term brightening of Mars surface albedos over the course of this 2001 global dust storm, which are most dramatic within the relatively dark surface regions of the southern low latitudes. For example, the 23°S, 291°W region of Figure 22 exhibits albedos in the range of 0.10 prior to this storm, as compared to the value of 0.31 derived in the midst of the storm. Similarly, the surface albedos at 7°N, 21°W and 30°N, 290°W (Figure 22) brightened to values of 0.12 and 0.32 from prior values of 0.08 and 0.27, respectively. A more detailed study of EPF-corrected surface solar band albedos as obtained from the full set of EPF fits will be presented in a future paper.

4. Conclusions

[46] Roughly 350 separate TES solar band EPF sequences have been fit employing a multiple scattering radiative transfer code with aerosol scattering properties (single scattering phase function and albedo) appropriate to the observed range of EPF emission and phase angle scattering, and the relative depths of 9 μm dust and 12 μm ice absorptions present in coincident TES measurements of thermal IR spectra. The seasonal (L_S) and latitudinal (45°S–45°N) variations of total aerosol (dust and ice) optical depth are derived for a full Mars year (1999–2001). Minimum optical depths of 0.2–0.3 are observed over the L_S range 0–140° outside of the aphelion cloud belt. Within this 10°S–30°N cloud feature, ice aerosol concentrations lead to 0.4–0.5 average total aerosol optical depths. Aerosol optical depths show abrupt global increases at L_S = 200° and 320° associated with regional dust storm activity. The aphelion cloud belt disappears abruptly at L_S = 145°. The effective wavelength of the TES solar band measurements is shown to be red visible light (λ_{eff} = 0.7 μm, with significant weighting over 0.4–1.5 μm). The range in best-fit single scattering phase functions for dust aerosols provides good agreement with the Pathfinder-based results of *Tomasko et al.* [1999] and previous IRTM EPF studies [*Clancy and Lee*, 1991]. Similarly, a best-fit dust single

scattering albedo of $0.92^{+0.2}_{-0.1}$ demonstrates good agreement with dust ssa retrievals by *Tomasko et al.* [1999]) and *Ockert-Bell et al.* [1997].

[47] Comparison of TES solar band aerosol optical depths to thermal infrared optical depths retrieved by *Smith et al.* [2001] show distinctive L_S/latitudinal variations in visible/IR optical depth ratios for both dust and ice aerosols. In particular, low visible/IR ratios ($\leq$1.5) are present within the aphelion ice cloud belt, and high visible/IR ratios ($\geq$2.5) for dust aerosols over L_S = 60–200°. These variations in ice optical depth ratios correlate with distinctive variations in ice aerosol single scattering phase functions, and lead to the definition of two Mars ice cloud populations. Type 1 ice clouds exhibit small particle sizes with diagnostic backscattering peaks, and are prevalent at mid southern latitudes during the aphelion season and as high-altitude hazes in all seasons. In contrast, type 2 ice clouds exhibit larger particles sizes and are more forward scattering, with a distinctive minimum in the their single scattering phase functions at 70–100° phase angles. Within the latitude range studied (45°S–45°N), type 2 ice clouds are restricted to 10°S–30°N latitudes and L_S = 40–140°. As such, type 2 ice clouds correlate with low-altitude water vapor saturation conditions and northern subtropical vertical advection within the aphelion solstice Hadley circulation [*Clancy et al.*, 1996].

[48] Quantitative dust and ice aerosol particle sizes are derived from a subset (~50) of the solar band EPF fits, in which detailed multiple scattering fits to coincident TES thermal IR spectral observations are performed [*Wolff and Clancy*, 2003]. In these cases, aerosol particle sizes independently determined from quantitatively accurate visible/IR optical depth ratios (here) and IR spectral fits [*Wolff and Clancy*, 2003] are compared, providing particularly sensitive definitions of particle size variations among Mars ice and dust aerosols. Type 1 ice aerosols exhibit a significant range of particle sizes (r_{eff} = 1–2 μm), which are distinctly smaller than determined for type 2 ice particle sizes (r_{eff} = 3–4 μm). Typical dust particle sizes found here (r_{eff} = 1.5 ± 0.1 μm) agree with Pathfinder measurements [*Tomasko et al.*, 1999] and reanalyses of Viking observations [*Clancy et al.*, 1995; *Pollack et al.*, 1995]. However, dust particle sizes also exhibit significant variations, contrary to previous inferences [e.g., *Toon et al.*, 1977; *Tomasko et al.*, 1999]. In particular, very small dust particle sizes (r_{eff} = 1.0 ± 0.2 μm) appear common over northern latitudes for the seasonal ranges L_S = 40–200° and 320–340°, and significantly larger dust particle sizes (r_{eff} = 1.8–2.5 μm) were present at southern latitudes during the 2001 global dust storm [see also *Wolff and Clancy*, 2003].

[49] Two limitations of the present analysis regard the sparse spatial and seasonal coverages of the EPF analysis (including lack of coverage above 45° latitudes), and a complete lack of vertical profile information. Subsequent EPF analyses will adopt automated solar band and thermal IR spectral fitting algorithms to provide much denser spatial and temporal coverages, including high-latitude analyses. In addition, TES limb observations of solar band and thermal IR spectral radiances promise a unique opportunity to profile ice and dust aerosol properties. *Conrath et al.* [2000] have retrieved temperature profiles from TES 15 μm limb radiances, as a necessary prelude to quantitative analysis of TES limb aerosol radiances in the IR. Analysis of TES limb profile observations in concert with co-located EPF observations further aids vertical profile coverage of aerosols into the bottom atmospheric scale height, where high limb optical depths prevent retrievals even under low aerosol loading conditions. Aerosol particle sizes and number densities for dust and ice components undoubtedly vary with altitude with features diagnostic of microphysics and atmospheric dynamics/transport [e.g., *Jaquin et al.*, 1986; *Chassefiere et al.*, 1992; *Montmessin et al.*, 2002; *Murphy et al.*, 1993; *Rodin et al.*, 1999].

[50] **Acknowledgments.** We are indebted to the excellent TES operations staff, particularly for the constant dedication and skillful directions of Kelly Bender and Kim Murray in the collection of these TES EPF data. We also acknowledge constant support from the GSFC TES team with EPF measurement strategy and data analysis, including an especially valuable collaboration with Dr. Michael Smith. Grant support for this work was provided by the MGS mission program (JPL contract 1220477) and by the Mars Data Analysis Program (MDAP grant NAG5-10662).

References

Cantor, B. A., P. B. James, M. Caplinger, and M. J. Wolff, Martian dust storms: 1999 Mars Orbiter Camera observations, *J. Geophys. Res.*, *106*, 23,653–23,687, 2001.

Chassefiere, E., J. E. Blamont, V. A. Krasnopolsky, O. I. Korablev, S. K. Atreya, and R. A. West, Vertical structure and size distributions of Martian aerosols from solar occultation measurements, *Icarus*, *97*, 46–69, 1992.

Christensen, P. R., et al., Initial results from the Mars Global Surveyor Thermal Emission Spectrometer experiment, *Science*, *279*, 1682–1685, 1998.

Christensen, P. R., et al., Mars Global Surveyor Thermal Emission Spectrometer experiment: Investigation description and surface science results, *J. Geophys. Res.*, *106*, 23,823–23,876, 2001.

Clancy, R. T., and S. W. Lee, A new look at dust and clouds in the Mars atmosphere: Analysis of emission-phase-function sequences from global Viking IRTM observations, *Icarus*, *93*, 135–158, 1991.

Clancy, R. T., S. W. Lee, G. R. Gladstone, W. W. McMillan, and T. Rousch, A new model for Mars atmospheric dust based upon analysis of ultraviolet through infrared observations from Mariner 9, Viking, and Phobos, *J. Geophys. Res.*, *100*, 5251–5264, 1995.

Clancy, R. T., A. W. Grossman, M. J. Wolff, P. B. James, Y. N. Billawala, B. J. Sandor, S. W. Lee, and D. J. Rudy, Water vapor saturation at low altitudes around Mars aphelion: A key to Mars climate?, *Icarus*, *122*, 36–62, 1996.

Clancy, R. T., B. J. Sandor, M. J. Wolff, P. R. Christensen, M. D. Smith, J. C. Pearl, B. J. Conrath, and R. J. Wilson, An intercomparison of ground-based millimeter, MGS TES, and Viking atmospheric temperature measurements: Seasonal and interannual variability of temperatures and dust loading in the global Mars atmosphere, *J. Geophys. Res.*, *105*, 9553–9572, 2000.

Colburn, D., J. Pollack, and R. Haberle, Diurnal variations in optical depth at Mars, *Icarus*, *79*, 159–189, 1989.

Conrath, B. J., J. C. Pearl, M. D. Smith, W. C. Maquire, P. R. Christensen, S. Dason, and M. S. Kaelberer, Mare Global Surveyor Thermal Emission Spectrometer (TES) observations: Atmospheric temperatures during aerobraking and science phasing, *J. Geophys. Res.*, *105*, 9509–9520, 2000.

Curran, R. J., B. J. Conrath, R. A. Hanel, V. G. Kunde, and J. C. Pearl, Mars: Mariner 9 spectroscopic evidence for H_2O clouds, *Science*, *182*, 381–383, 1973.

Deirmidjian, D., Scattering and polarization properties of water clouds and hazes in the visible and infrared, *Appl. Opt.*, *3*, 187–202, 1964.

French, R. G., P. J. Gierasch, B. D. Popp, and R. J. Yerdon, Global patterns in cloud forms on Mars, *Icarus*, *45*, 468–493, 1981.

Gierasch, P. J., and R. M. Goody, The effect of dust on the temperature structure of the Martian atmosphere, *J. Atmos. Sci.*, *29*, 400–402, 1972.

Glenar, D. A., R. E. Samuelson, J. C. Pearl, G. L. Bjoraker, and D. Blaney, Spectral imaging of Martian water ice clouds and their diurnal behavior during the 1999 aphelion season (L_S = 130°), *Icarus*, *161*, 297–318, 2003.

Haberle, R. M., C. B. Leovy, and J. B. Pollack, Some effects of global dust storms on the atmospheric circulation of Mars, *Icarus*, *50*, 322–367, 1982.

Haberle, R. M., M. M. Joshi, J. R. Murphy, J. R. Barnes, J. T. Schofield, G. Wilson, M. Lopez-Valverde, J. L. Hollingsworth, A. F. C. Bridger, and J. Schaeffer, General circulation model simulations of the Mars

Pathfinder atmospheric structure investigation/meteorological data, *J. Geophys. Res.*, *104*, 8957–8974, 1999.
Hanel, R. A., B. Conrath, W. Hovis, V. Kunde, P. Lowman, W. Maquire, J. Pearl, J. Pirraglia, C. Prabhakara, and B. Schlachman, Investigation of the Martian environment by infrared spectroscopy on Mariner 9, *Icarus*, *17*, 423–442, 1972.
Ivanov, A. B., and D. O. Muhleman, Opacity of the Martian atmosphere from Mars Orbiter Laser Altimeter (MOLA) observations, *Geophys. Res. Lett.*, *25*, 4417–4420, 1998.
Jaquin, F., P. G. Gierasch, and R. Kahn, The vertical structure of limb hazes in the Martian atmosphere, *Icarus*, *68*, 442–461, 1986.
Kahn, R., The spatial and seasonal distribution of Martian clouds, and some meteorological implications, *J. Geophys. Res.*, *89*, 6671–6688, 1984.
Kahn, R., T. Z. Martin, R. W. Zurek, and S. W. Lee, The Martian dust cycle, in *Mars*, edited by H. H. Kieffer, et al., pp. 1017–1053, Univ. of Ariz. Press, Tucson, 1992.
Martin, L. J., and R. W. Zurek, An analysis of the history of dust activity on Mars, *J. Geophys. Res.*, *98*, 3221–3246, 1993.
Martin, T. Z., Thermal infrared opacity of the Mars atmosphere, *Icarus*, *66*, 2–21, 1986.
Michelangeli, D. V., O. B. Toon, R. M. Haberle, and J. B. Pollack, Numerical simulations of the formation and evolution of water ice clouds in the Martian atmosphere, *Icarus*, *100*, 261–285, 1993.
Mishchenko, M. I., L. D. Travis, R. A. Kahn, and R. A. West, Modeling phase functions for dustlike tropospheric aerosols using a shape mixture of randomly oriented polydisperse spheroids, *J. Geophys. Res.*, *102*, 16,831–16,848, 1997.
Montmessin, F., P. Rannou, and M. Cabane, New insights into Martian dust distribution and water-ice cloud microphysics, *J. Geophys. Res.*, *107*(E6), 5037, doi:10.1029/2001JE001520, 2002.
Murphy, J. R., R. M. Haberle, O. B. Toon, and J. B. Pollack, Martian global dust storms: Zonally symmetric numerical simulations including size-dependent particle transport, *J. Geophys. Res.*, *98*, 3197–3220, 1993.
Ockert-Bell, M. E., J. F. Bell III, J. B. Pollack, C. P. McKay, and F. Forget, Absorption and scattering properties of the Martian dust in the solar wavelengths, *J. Geophys. Res.*, *102*, 9039–9050, 1997.
Pang, K., and C. W. Hord, Mariner 9 ultraviolet spectrometer experiment: 1971 Mars' dust storm, *Icarus*, *18*, 481–488, 1973.
Pearl, J. C., M. D. Smith, B. J. Conrath, J. L. Bandfield, and P. R. Christensen, Observations of Martian ice clouds by the Mars Global Surveyor Thermal Emission Spectrometer: The first year, *J. Geophys. Res.*, *106*, 12,325–12,338, 2001.
Pollack, J., D. Colburn, F. M. Flaser, R. Kahn, C. Carlson, and D. Pidek, Properties and effects of dust particles suspended in the Martian atmosphere, *J. Geophys. Res.*, *84*, 2929–2945, 1979.
Pollack, J. B., M. E. Ockert-Bell, and M. K. Sheppard, Viking lander analysis of Martian atmospheric dust, *J. Geophys. Res.*, *100*, 5235–5250, 1995.
Rodin, A. V., O. I. Korablev, and V. I. Moroz, Vertical distribution of water in the near-equatorial troposphere of the Martian atmosphere, *Icarus*, *125*, 212–229, 1997.
Rodin, A. V., R. T. Clancy, and R. J. Wilson, Dynamical properties of Mars water ice clouds and their interactions with atmospheric dust and radiation, *Adv. Space. Res.*, *23*, 1577–1585, 1999.
Smith, M. D., J. C. Pearl, B. J. Conrath, and P. R. Christensen, Mars Global Surveyor Thermal Emission Spectrometer (TES) observations of dust opacity during aerobraking and science phasing, *J. Geophys. Res.*, *105*, 9539–9552, 2000.
Smith, M. D., J. C. Pearl, B. J. Conrath, and P. R. Christensen, Thermal emission spectrometer results: Mars atmospheric thermal structure and aerosol distribution, *J. Geophys. Res.*, *106*, 23,929–23,945, 2001.
Smith, M. D., B. J. Conrath, J. C. Pearl, and P. R. Christensen, Thermal Emission Spectrometer observations of Martian planet-encircling dust storm 2001A, *Icarus*, *157*, 259–263, 2002.
Smith, P. H., and M. Lemmon, Opacity of the Martian atmosphere measured by the Imager for Pathfinder, *J. Geophys. Res.*, *104*, 135–158, 1999.
Stamnes, K., S. C. Tsay, W. Wiscombe, and K. Jayaweera, Numerically stable algorithm for discrete ordinate method radiative transfer in multiple scattering and emitting layered media, *Appl. Opt.*, *27*, 2502–2509, 1988.
Tamppari, L. K., R. W. Zurek, and D. A. Paige, Viking era water ice clouds, *J. Geophys. Res.*, *105*, 4087–4107, 2000.
Thorpe, T. E., A history of Mars atmospheric opacity in the southern hemisphere during the Viking extended mission, *J. Geophys. Res.*, *84*, 6663–6683, 1979.
Thorpe, T. E., Mars atmospheric opacity in the northern hemisphere by Viking Orbiter imaging, *J. Geophys. Res.*, *86*, 11,419–11,429, 1981.
Toigo, A. D., and M. I. Richardson, Seasonal variation of aerosols in the Martian atmosphere, *J. Geophys. Res.*, *105*, 4121–4190, 2000.
Tomasko, M. G., L. R. Doose, M. Lemmon, P. H. Smith, and E. Wegryn, Properties of dust in the Martian atmosphere from the Imager on Mars Pathfinder, *J. Geophys. Res.*, *104*, 8987–9008, 1999.
Toon, O. B., J. B. Pollack, and C. Sagan, Physical properties of the particles composing the Martian dust storm of 1971, *Icarus*, *30*, 663–696, 1977.
Warren, S. G., Optical constants of ice from the ultraviolet to the microwave, *Appl. Opt.*, *23*, 1206–1225, 1984.
Wilson, R. J., A general circulation model simulation of the Martian polar warming, *Geophys. Res. Lett.*, *24*, 123–127, 1997.
Wolff, M. J., and R. T. Clancy, Constraints on the size of Martian aerosols from Thermal Emission Spectrometer observations, *J. Geophys. Res.*, *108*, doi:10.1029/2003JE002057, in press, 2003.
Wolff, M. J., R. T. Clancy, and K. M. Pitman, On the nature of Martian composite dust/water-ice aerosols, *Bull. Am. Astron. Soc.*, *32*, 1104, 2000.
Zurek, R. W., Martian great dust storms: An update, *Icarus*, *50*, 288–310, 1982.

P. R. Christensen, Department of Geology, Arizona State University, Tempe, AZ 85287, USA.
R. T. Clancy and M. J. Wolff, Space Science Institute, 3100 Marine Street, Suite A353, Boulder, CO 80303-1058, USA. (clancyr@colorado.edu)